1

Mechanics Design of Flexible Sensors

Li Yuhang[1], *Zhao Zhao*[2], *and Wu Wenbin*[1]

[1] *Beihang University (BUAA), Institute of Solid Mechanics, School of Aeronautic Science and Engineering, XueYuan Road, HaiDian District, Beijing 100191, P.R. China*
[2] *China Special Equipment Inspection and Research Institute, HePing Street, ChaoYang District, Beijing 100029, P.R. China*

1.1 Design of Stretchable Flexible Device Structure

The physical synthesis of fragile inorganic semiconductor materials has been realized with the development of nanofabrication technology, which leads to explosive growth in the research of high-performance stretchable flexible devices [1–3]. Due to their excellent flexibility, ductility, and better mechanical properties, inorganic semiconductor materials can form three-dimensional (3D) structures through self-assembly or indirect guidance, including tubular, wrinkled, buckling, and other delicate structures [4, 5]. Inorganic semiconductor materials in lines, bands, films, sheets, and strips can be obtained [6]. These materials can be used for high-performance transistors and circuit components of flexible, stretchable electronic devices. Integrating these materials into flexible substrates to prepare high-performance flexible electronic devices has become an important research issue. Therefore, relevant scholars have proposed different mechanical structure guidance strategies based on the principles of mechanics, including the ripple method, island bridge connection method, etc., which meet the high-performance requirements of electronic devices for complex surfaces [7].

1.1.1 Ripple Method

Buckling means the instability and failure of the structure. However, the design method of controllable buckling can effectively improve the ability of flexible electronics to resist tensile and compressive failure. Based on the buckling principle, the ripple method can make the flexible substrate and the film attached to it produce large wavy deformation simultaneously through the pre-stretching and strain release of the flexible substrate to adapt to and withstand more significant deformation [8].

Soft Electronics for Diagnosis, Therapy, and Integrated Systems, First Edition.
Edited by Xinge Yu, Jiyu Li, Ya Huang, and Enming Song.

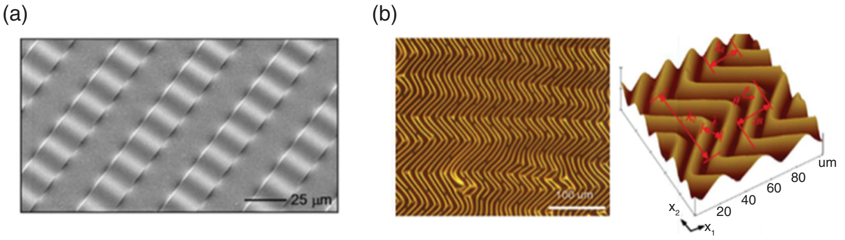

Figure 1.1 (a) Scanning electron microscopy (SEM) images of wavy Si ribbons on PDMS substrates. (b) Optical microscopy images and atomic force microscopy images of wavy Si nanofilms. Source: Song et al. [2]/with permission of AIP Publishing.

There are three main preparation methods for corrugated structure: substrate pre-strain releasing, closed colloidal solution expansion, and ultraviolet radiation method [9–11]. The substrate pre-strain release method mainly uses single-crystal etching to pattern the silicon film. The silicon film array is placed on the pre-stretched polydimethylsiloxane (PDMS) substrate based on the transfer printing. Then, the pre-stretched strain of the substrate is released to generate compressive stress, and a corrugated silicon film-PDMS double-layer structure is obtained, as shown in Figure 1.1.

Yu et al. [10] from Arizona State University fabricated a novel stretchable temperature sensor using the substrate pre-strain release method. Figure 1.2 shows that the ultra-thin single-crystal silicon film was prepared by traditional lithography technology. The Cr-Au thin layer thermistor was prepared by the sputtering deposition method and patterned by the boosting method. Then, the single-crystal silicon band was prepared by reactive ion etching as the bonding layer between the thermistor and the rubber substrate. Based on the van der Waals force, the thermistor-monocrystalline silicon adhered to PDMS is peeled off from the silicon-on-insulator (SOI) film, and another PDMS substrate with pre-strain after radiation treatment is prepared. Finally, the pre-strain is released to obtain a corrugated flexible temperature sensor device.

Yang et al. [9] used a closed colloidal solution expansion method to prepare a PDMS flexible double-layer structure with wavy wrinkled films and proposed a strategy to control wavy patterns and characteristic wavelengths to achieve various applications of corrugated structures, including adjustable adhesion, wetting, microfluidics, and microlens arrays. Figure 1.3 shows that the solvent or monomer solution is used to expand and seal the elastic-plastic polymer or hydrogel film. Because the bottom of the film is connected to the rigid substrate and cannot deform, an anisotropic osmotic pressure is generated along the thickness direction of the film. When the net pressure exceeds the critical pressure, the outer surface of the outer film will buckle and form a corrugated structure pattern (Figure 1.4).

Yu and Jiang [11] from Arizona State University processed the pre-stretched PDMS substrate by ultraviolet radiation to prepare an SIO_2 film with a wavy structure. The effects of pre-strain, radiation duration, and modulus on the wavy profile were obtained, and the accuracy of the mechanical analysis was confirmed

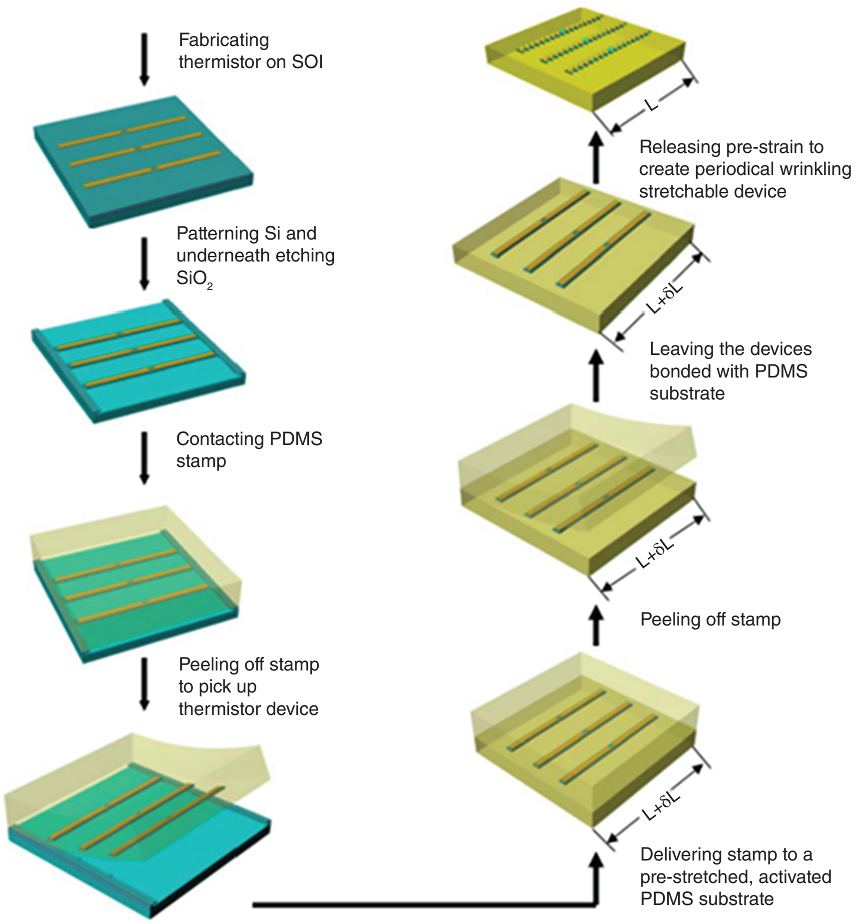

Figure 1.2 Pre-strain preparation method of corrugated structure. Source: Yu et al. [10]/ with permission of AIP Publishing.

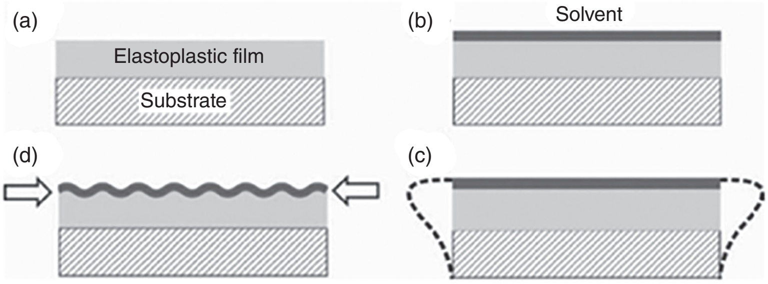

Figure 1.3 (a–d) Schematic diagram of corrugated structure prepared by closed colloidal solution expansion method. Source: Yang et al. [9]/with permission of John Wiley & Sons.

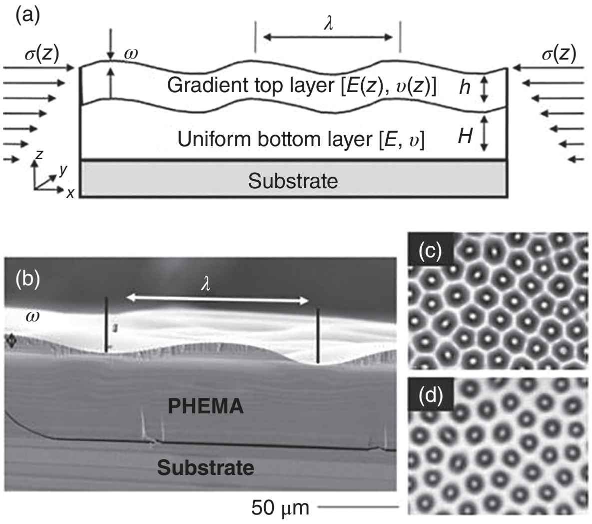

Figure 1.4 (a–d) Schematic diagram of film layer structure with modulus gradient prepared by photocrosslinking method. Source: Yang et al. [9]/with permission of John Wiley & Sons.

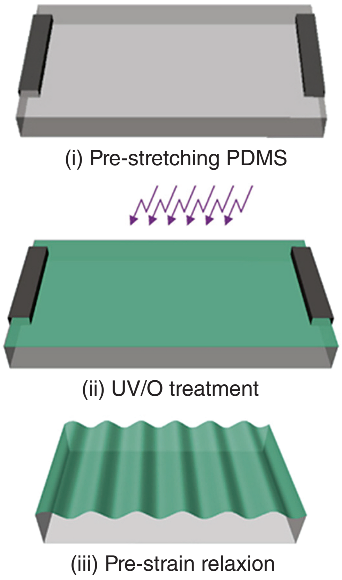

Figure 1.5 The steps of preparing corrugated structure by ultraviolet radiation. Source: Yu and Jiang [11]/with permission of Elsevier.

by experimental comparison. The researchers first prepared a pre-stretched PDMS substrate and placed it under the radiation of an ultraviolet lamp in the atmospheric environment. The chemical composition of PDMS can be changed by reacting with oxygen. After reaching a sufficient exposure time, the pre-strained PDMS surface will produce a wavy structure (Figure 1.5).

To further study the buckling properties of corrugated structures in stretchable electronic devices, scholars have investigated through experiments, theories, and finite element methods and made a reasonable explanation for the formation and evolution mechanism of periodic buckling corrugated structures on macro- and

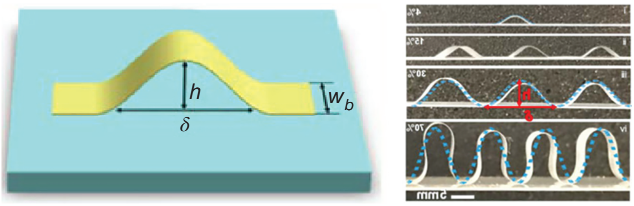

Figure 1.6 Geometric diagram of buckling delamination of corrugated structure. Source: Zhang and Yin [12]/with permission of Elsevier.

microscales [8–10, 12–21]. Zhang and Yin [12] from Temple University carried out related research on the periodic delamination mechanism of spontaneous buckling of thin films on flexible substrates under significant compression. Firstly, the geometric evolution mechanical model of the periodic corrugated structure is established based on the energy method and verified by experiments and finite element simulation. According to the size of the compressive strain, the geometric deformation process of the corrugated structure can be divided into three stages: the generation of buckling delamination under minor compression conditions, the expansion of buckling delamination under medium compression conditions, and the post-buckling phenomenon of delamination stopping under extensive compression conditions. In the experimental study, a thin metal film Au (thickness of 40 nm) was deposited on a uniaxially pre-stretched PDMS (thickness of 2 mm) substrate. The delamination process of the buckling surface morphology was characterized by scanning electron microscopy to evaluate the evolution process of the microbuckling delamination release strain (Figure 1.6).

Considering the large deformation of the silicone rubber substrate, it is assumed that the film is an elastic thin plate and the substrate is a semi-infinite solid that satisfies the Neo-Hookean constitutive law. The total energy U_{tol} in the film-substrate system is composed of the tensile energy in the film U_{str}, the bending energy U_{bend}, the elastic energy in the substrate U_{sub}, and the adhesion energy between the film and the substrate U_{adh}, as shown in the following formula:

$$U_{tol} = U_{str} + U_{bend} + U_{sub} + U_{adh} \tag{1.1}$$

The tensile strain and bending energy of the film can be written as:

$$U_{bend} = \frac{1}{2}\int_s M_{\alpha\beta}\kappa_{\alpha\beta} dA \tag{1.2}$$

$$U_{str} = \frac{1}{2}\int_s \sigma_{\alpha\beta}\varepsilon_{\alpha\beta} t dA \tag{1.3}$$

The approximate relationship between the shape of the corrugated structure and the applied strain is $\varepsilon \approx \pi^2 h^2/4\delta^2$. So, the tensile strain energy in the film can be approximately ignored under the assumption of the nonexpandable film. The strain energy of nonlinear elastic substrate can be given as:

$$U_{sub} = \int_v W_s dV \tag{1.4}$$

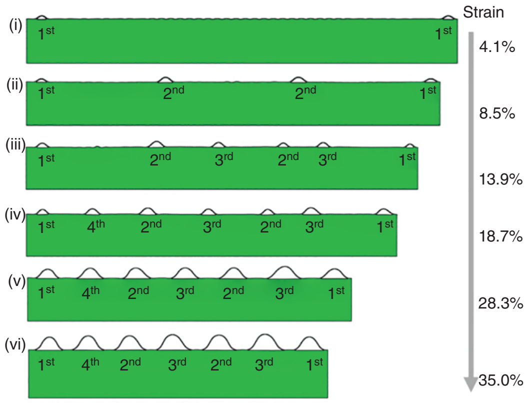

Figure 1.7 Finite element simulation structure of buckling delamination under different tensile levels. Source: Zhang and Yin [12]/with permission of Elsevier.

Since the strain energy in the substrate and the strain energy of the film delamination can be neglected, the effect of nonlinear buckling of the material in the elastic substrate on the buckling delamination morphology can be neglected (Figure 1.7).

Given the limitations of the original semi-infinite substrate model, Ma et al. [13] studied the buckling critical pre-strain of a finite-thickness substrate. The pre-strain is released and bonded to the polyimide film on the flexible substrate into a sinusoidal corrugated structure. The tensile stiffness of the substrate is much smaller than that of the film; the substrate cannot shrink back to the initial length after pre-strain release, so the film-substrate system may bend (Figure 1.8).

Based on the finite thickness substrate assumption, the critical pre-strain can be obtained as follows. The critical buckling strain of the polyimide film on the PDMS substrate increases with the ratio h/H of the film height to the substrate height, consistent with the finite element analysis (FEA) results.

Yan et al. [14] studied the mechanical buckling of thin films bonded to pre-strained finite-thickness substrates. The maximum strain analysis method and the critical

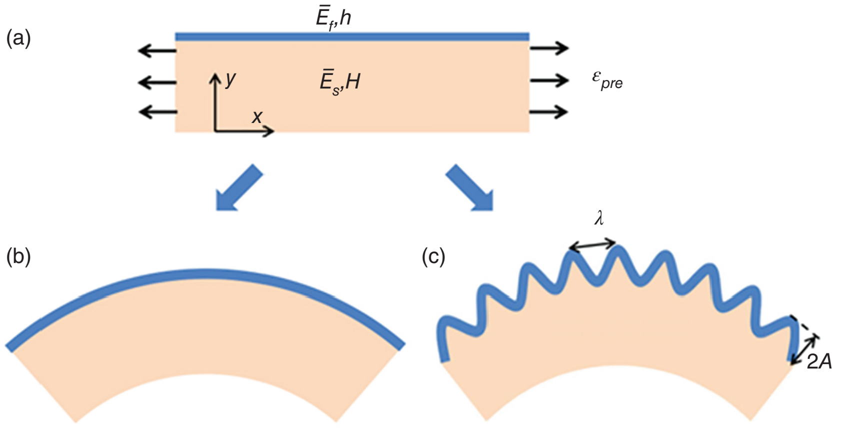

Figure 1.8 (a–c) Schematic diagram of corrugated-substrate buckling structure with finite thickness. Source: Ma et al. [13]/with permission of Royal Society of Chemistry.

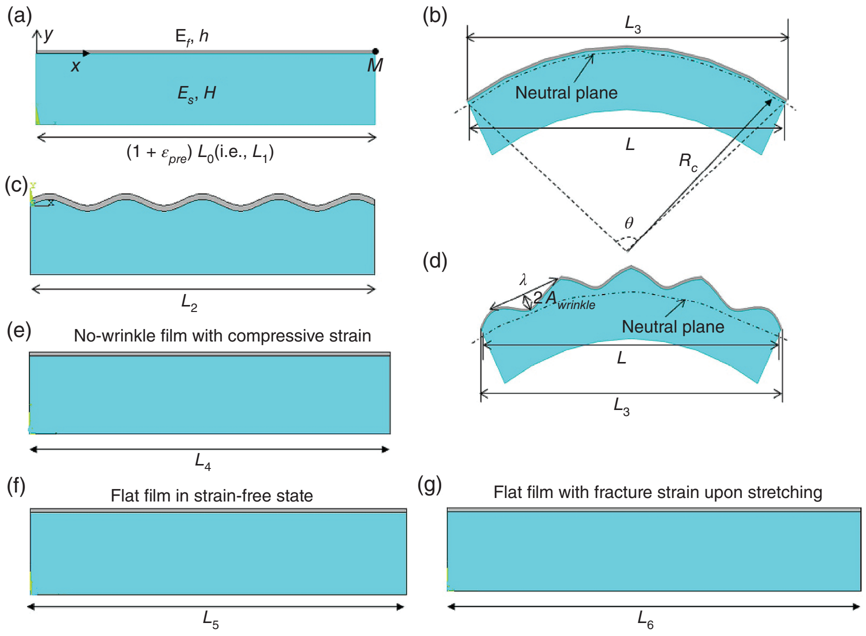

Figure 1.9 (a–g) Geometric diagram of buckling of the corrugated structure under different tensile levels. Source: Yan et al. [14]/with permission of Elsevier.

Figure 1.10 (a,b) Simplified mechanical model of buckling wrinkles. Source: Yan et al. [14]/with permission of Elsevier.

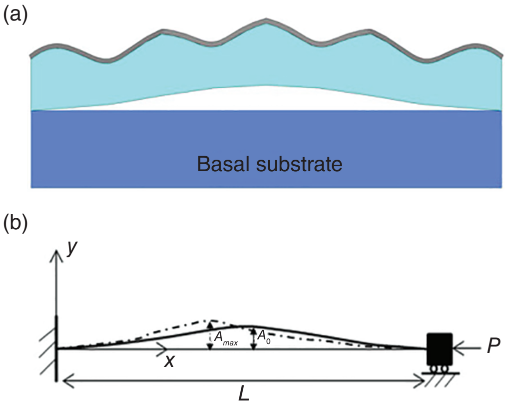

buckling load analysis model were established, respectively, and the maximum tensile and compressibility evaluation criteria of the buckling structure were established (Figures 1.9 and 1.10).

The stretchability of the curved corrugated structure is:

$$\delta_{stretch} = \frac{L_6 - L_3}{L_3} \times 100\% \tag{1.5}$$

where L_6 is the maximum tensile length, and the length between the two ends of the top film is L_3, as shown in Figure 1.9, which can be approximated as the length of the two ends of the neutral surface of the curved film/substrate structure. According to the buckling analysis, the critical buckling load is positive only when the thickness ratio of the substrate/film exceeds the critical value, and the larger thickness ratio makes the critical load larger. The maximum strain of the film mainly depends on the substrate and strain. Based on the critical buckling load and maximum strain criterion, the maximum compressibility based on buckling analysis and maximum stress analysis is 7% and 20%, respectively.

Jiang et al. [15] from Arizona State University studied the post-buckling mechanical behavior of corrugated structures based on the energy method and obtained the buckling wavelength and peak value of the ripple. When the applied strain reaches the critical strain, the buckling wavelength increases, the amplitude disappears, and the film strain is equal to the critical strain. The additional applied strain relaxes the film and eventually stretches to a breaking point.

The above studies focus on brittle materials on soft elastic substrates and endow the substrate-film system with stretchable mechanical properties through controllable buckling. However, the typical elastomer is permeable to the fluid, so it cannot provide a waterproof function. Moreover, since the primary system mechanical strength of the soft substrate usually cannot meet the practical application, a double-layer substrate is introduced. That is, there is a soft layer on the relatively hard layer in the substrate, which can ensure the mechanical properties of the equipment without losing its stretchability (Figure 1.11).

Cheng et al. [16] established a simple analytical model of a rigid film on a double-layer substrate. The amplitude and wavelength of the buckling corrugated structure are obtained by the energy method. The Young's modulus of the top substrate layer is more critical than the Young's modulus of the bottom substrate layer for the wavelength, amplitude, and maximum strain of the buckling berth structure.

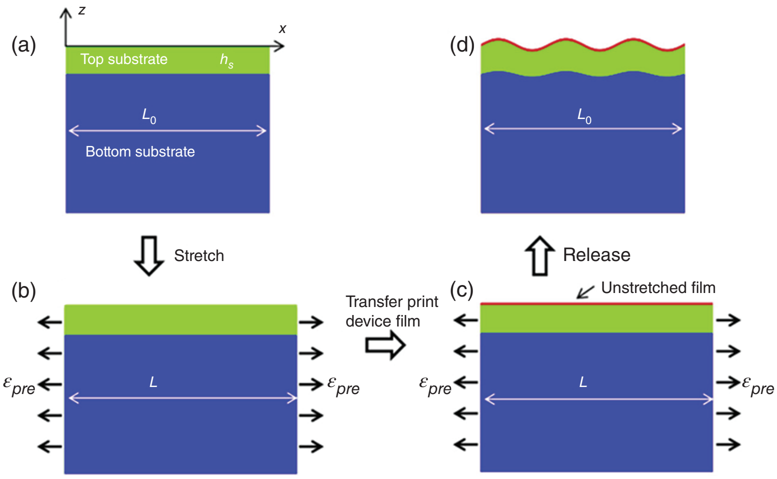

Figure 1.11 (a–d) Schematic diagram of double substrate soft layer film-substrate system. Source: Cheng et al. [16]/with permission of Elsevier.

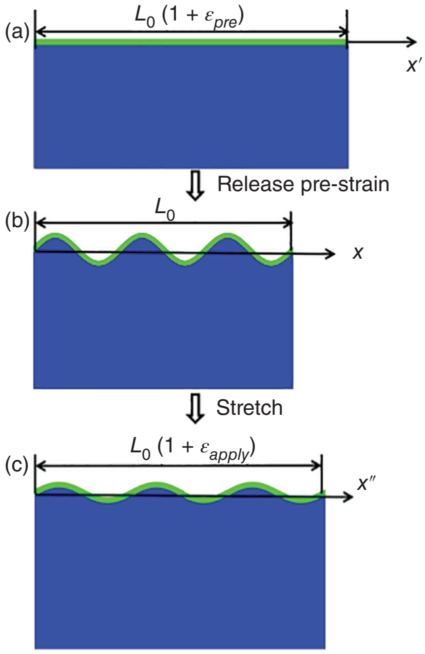

Figure 1.12 (a–c) Structure diagram of nonlinear corrugated-substrate system. Source: Cheng et al. [16]/with permission of Elsevier.

For the amplitude and wavelength of the buckled corrugated structure, Cheng and Song [17] from the University of Miami also considered the nonlinear constitutive model of the pre-strained substrate under different conditions: (i) the geometric change of the film/substrate system in the nonstrain state; (ii) the finite strain of the substrate has a nonlinear strain-displacement relationship; (iii) the nonlinear constitutive model of the substrate. The results show that the post-buckling amplitude of the film decreases with the increase in the applied strain. In contrast, the wavelength increases with the increase in the applied strain, and the finite geometric change plays a dominant role in the post-buckling (Figure 1.12).

Song et al. [18] from the University of Illinois used the perturbation method to analyze the mechanical properties of the buckling film on the flexible substrate. To further study the influence parameters of the buckling mechanical behavior of thin films on flexible substrates, Jiang et al. [20] from Arizona State University conducted systematic experiments and analysis on the buckling behavior of finite-width rigid films on flexible substrates. The results show that the amplitude and wavelength of the buckling film increase with the increase in the film width (Figure 1.13).

The above studies assume that the buckling structure of the film is a sinusoidal buckling geometry. Chen et al. [21] abandoned the original sinusoidal geometric buckling assumption and proposed a new theoretical model to describe the deformation of the buckling film. The mechanical model shows that the previous mechanical model overestimates the deflection and curvature of the film. The results can provide design guidance for many applications, such as stretchable electrons to micro-nanoscale surface patterns and precision metrology.

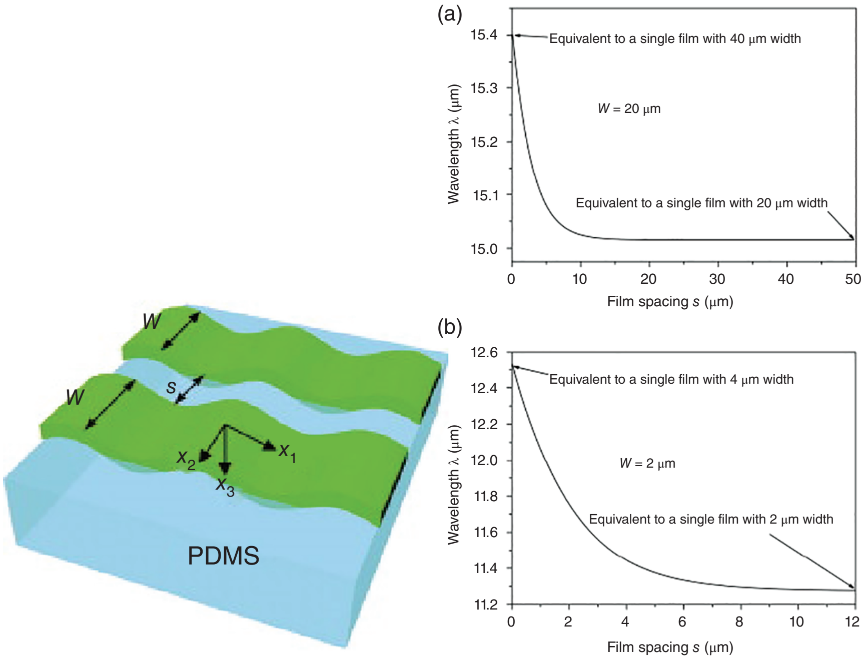

Figure 1.13 Effect of membrane spacing on buckling amplitude. Source: Jiang et al. [20]/ with permission of Elsevier.

1.1.2 Island Bridge Structure-Curved Line

To further improve the stretchability of flexible electronic devices, Song et al. [22] proposed a noncoplanar grid design, which uses a semiconductor island and an arc line connected to an elastic substrate. The maximum strain on the arc line and the island is predicted, and the tensile row and compressibility of the entire system are studied. The maximum strain in the arc line decreases with the increase in the pre-strain. Since the island devices are mostly rigid electronic components, the elastic modulus is much larger than the arc line structure. So, the peak strain in the island is much smaller than the strain in the arc line (Figure 1.14).

Li et al. [23] established an analytical mechanical model of the island bridge structure. Based on the unified scaling law, the relationship between the normalized maximum strain of the island bridge structure and the strain of the substrate is revealed, which provides a theoretical basis for the fracture safety of stretchable electronic components (Figure 1.15).

Among them is the scaling law of the maximum strain on the island:

$$\varepsilon_{island}^{\max} = \frac{E_{bridge} I_{bridge} t_{island}}{D L_{bridge}} f\left(\varepsilon_{pre}, \nu_{island}, \frac{b}{a}, \frac{ka^4}{D}\right) \tag{1.6}$$

According to the adhesion between the banded material and the substrate, there may be three de-deformation modes: global, local, and nonbuckling [24]. Wang et al. [25] established the critical length and thickness ratio of the arc-shaped banded

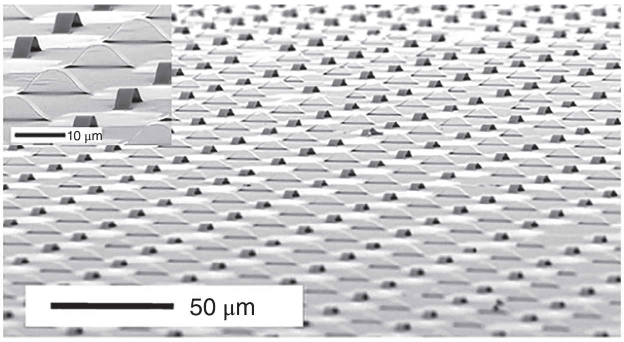

Figure 1.14 Noncoplanar arc line structure. Source: Song et al. [22]/with permission of AIP Publishing.

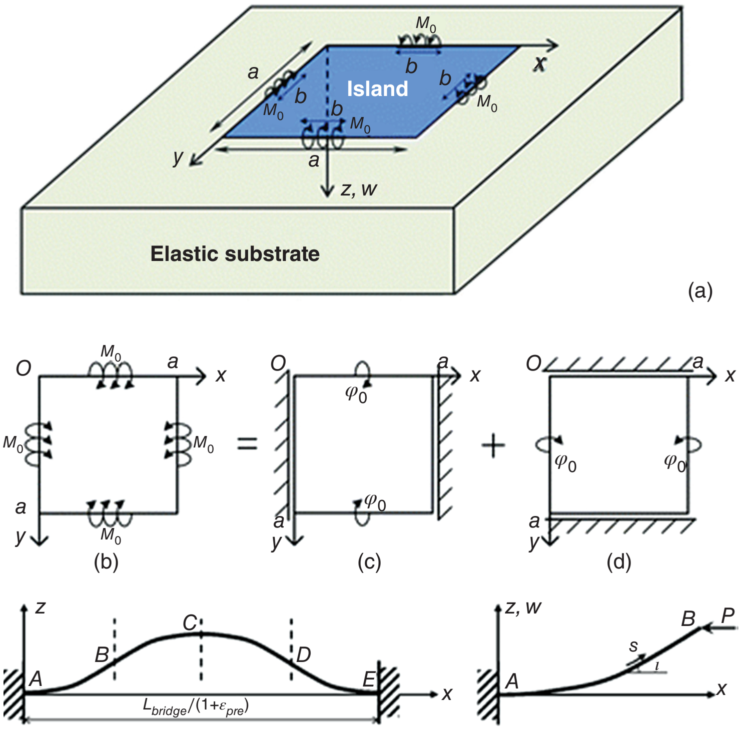

Figure 1.15 Loading mechanical model of the island on the substrate. Source: Li et al. [23]/with permission of Royal Society of Chemistry.

structure for the banded material structure that is selectively bonded to the elastic substrate, and global buckling can occur without material failure (Figure 1.16).

Wang and Wang [26] studied the four buckling modes of curved films. When the soft tissue shrinks, the electronic components are compressed and bent into various modes. Due to the different stiffness of the tissue and the degree of adhesion of the interface, buckling occurs. The phenomenon of delamination and the conditions for

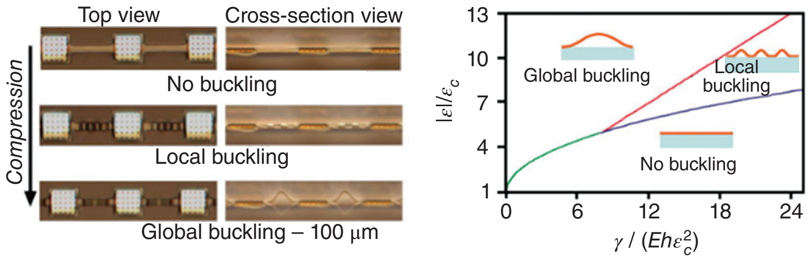

Figure 1.16 The three possible deformation modes of a filamentary ribbon. Source: Ko et al. [24]/with permission of John Wiley & Sons.

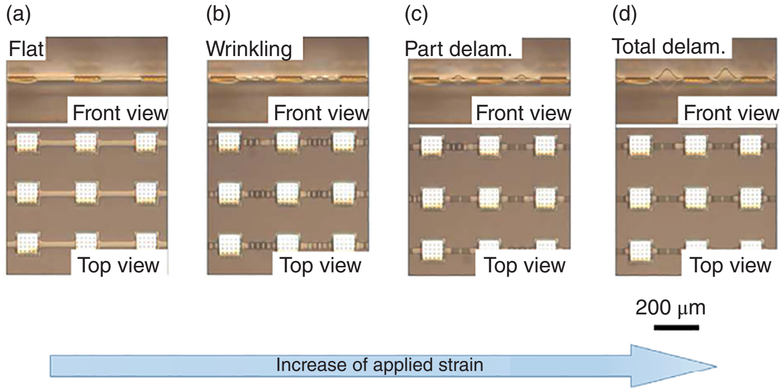

Figure 1.17 (a–d) Experimental diagrams of four buckling modes. Source: Wang and Wang [26]/with permission of Elsevier.

generating different buckling modes are verified theoretically and experimentally, as shown in Figure 1.17.

Various buckling modes can be divided into four modes, as shown in Figure 1.18:

(1) In the case of no compression to slight compression, the film does not buckle and remains flat;
(2) With the increase of compression, the film wrinkles at the top of the elastomer into multiple wavelets but does not delaminate from the interface, which we call the wrinkling mode;
(3) Under further compression, multiple waves are merged into one, resulting in partial delamination of the film from the interface, which is a partial delamination mode;
(4) The more considerable compression eventually leads to the complete delamination of the film from the interface, which is defined as the complete delamination mode in this study.

The island bridge structure with curved lines can be used for conformal packaging planes, such as placing silicon-based circuits on complex surfaces. Wang et al. [27] established a reliable method to predict the buckling mode of interconnected

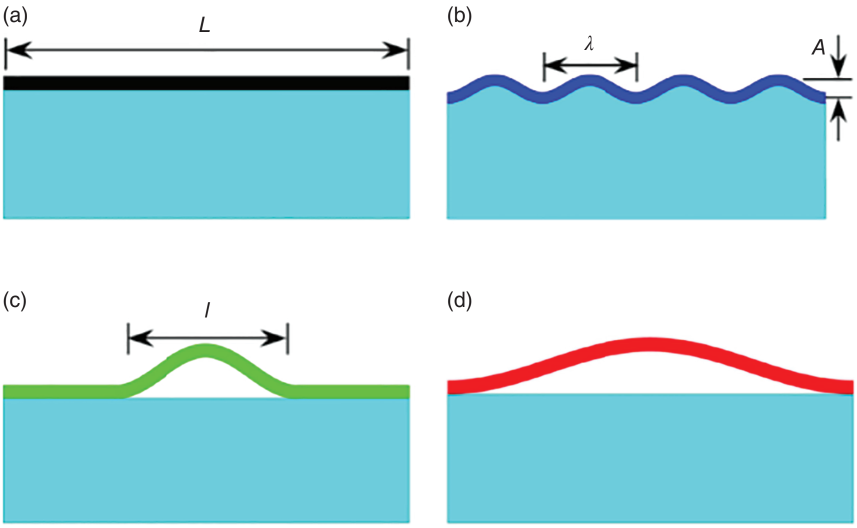

Figure 1.18 Four kinds of buckling mode diagram. (a) Flat. (b) Wrinkling. (c) Partial delamination. (d) Total delamination. Source: Wang and Wang [26]/with permission of Elsevier.

island-bridge structures on arbitrary axisymmetric surfaces. First, the stress distribution on the curved surface is obtained analytically. Then, the buckling modes of the interconnection bridge along different directions and different positions of the curve are determined by using the stress distribution. Finally, the maximum strain of the interconnection island bridge structure is analytically obtained using the stress distribution and buckling mode (Figure 1.19).

1.1.3 Island Bridge Structure-Serpentine Line

Compared with the wave structure and the island bridge structure connected by arc lines, the island bridge structure connected by serpentine lines can effectively solve the problem of insufficient island spacing and increase the effective coverage area of circuit components [28–35].

Widlund et al. [29] studied the influence of serpentine wire geometry on its stretchability and flexibility through theoretical, numerical, and experimental methods. The results show that the narrower the band, the larger the arc radius and arc angle, and the longer the arm length, the smaller the intrinsic strain and effective stiffness. When the arm length is close to infinity, the stretchability can be improved by several orders of magnitude (Figure 1.20).

Electronics for wearable applications require soft, flexible, and stretchable materials and designs to overcome the mechanical mismatch between the human body and the device. The critical requirement of this wearable electronic device is reliable operation with high performance and robustness in various deformations caused by motion. Son et al. [30] proposed materials and device design strategies for core components of wearable electronic products, such as transistors, charge trap

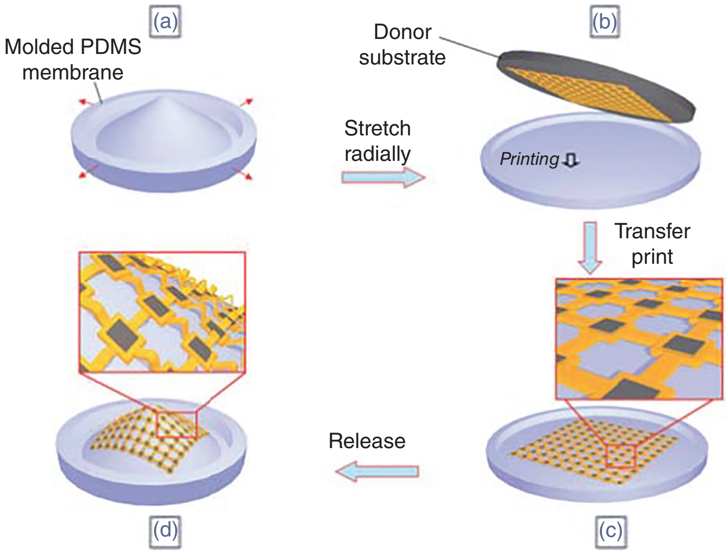

Figure 1.19 A schematic diagram of a conformal curved object wrapped by a compressible circuit grid structure and an elastic transfer element. Source: Wang et al. [27]/with permission of Royal Society of Chemistry.

floating gate memory cells, and various logic gates with stretchable shape factors (Figure 1.21).

Yang et al. [31] developed a low-cost, dehydrated manufacturing process to successfully integrate the brittle indium tin oxide (ITO) serpentine tape on a stretchable substrate. *In situ* electromechanical experiments measured the tensile properties of ITO ribbons. It was found that the tensile properties were not only related to the shape of the ribbons but also to the adhesion between the ribbons and the substrate. When the adhesion is weak, up to 200% stretchability can be achieved. When the adhesion is strong, a new failure mechanism is observed, which can be used for design criteria under different adhesion conditions (Figure 1.22).

Based on the finite deformation of the plane bending beam, Fan et al. [32] established an analytical model of serpentine connection. The FEA of serpentine interconnects with various geometric parameters is carried out to verify the established model. By comparing the predicted stretchability with the estimation of the linear model, the influence of finite deformation can be quantitatively studied. Both theoretical and numerical results show that the linear model can cause considerable overestimation for many serpentine interconnects with representative shapes. In addition, a simplified analytical solution of stretchability is obtained using the approximate model of the nonlinear effect (Figure 1.23).

Xiao et al. [33] studied the conformal design of island bridges on undevelopable surfaces, including the critical size and stiffness and the tensile requirements of bridges. First, the conformal model of the island on the surface of the torus is established to determine the relationship between the maximum size of the island and the surface curvature. The critical dimensionless width of the island is given, which

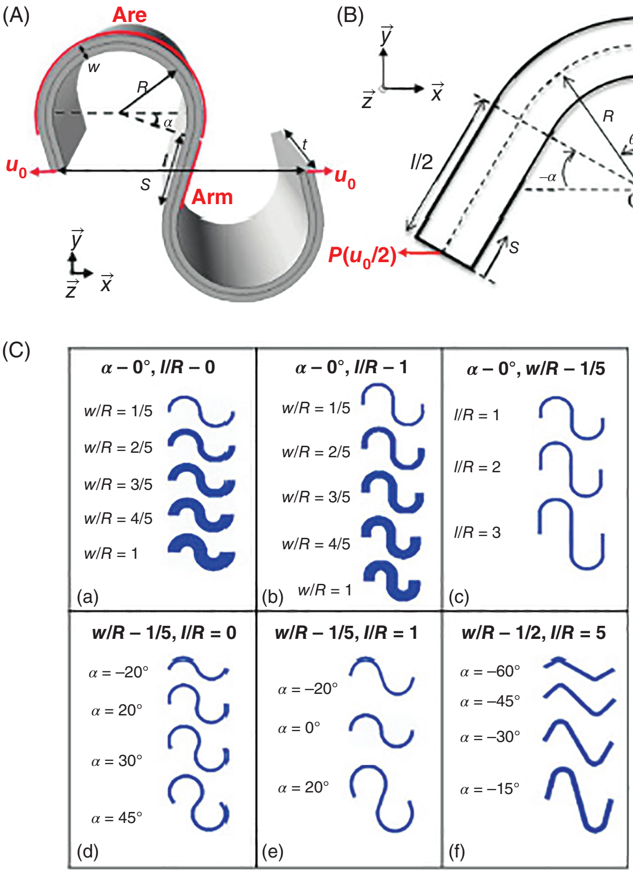

Figure 1.20 (A–C) Shape parameter diagram of snake-like geometric structure. Source: Widlund et al. [29]/with permission of Elsevier.

is a function of the thickness of the island, the interface adhesion energy, and the ratio of the two principal curvatures of the surface. Then, the FEA method is used to study the relationship between the tensile stiffness of the bridge and the geometric parameters to guide the deterministic assembly of the surface islands. Finally, the position-dependent bridge stretchability requirements are given by geometric mapping. This work will provide design rules for stretchable electronic devices fully compliant with nonexpandable surfaces (Figure 1.24).

Xu et al. [34] developed a 3D elastic membrane that accurately matches the epicardium of the heart by using 3D printing as a platform for multifunctional sensors with deformable arrays of electronic and optoelectronic components. This skin device completely suitably encapsulates the heart and has inherent elasticity to provide a mechanically stable biotic/biotic interface during a normal cardiac cycle (Figure 1.25).

Lithography-defined electrical interconnections with thin, filamentary serpentine layouts have been widely explored for stretchable electronics supported by elastic

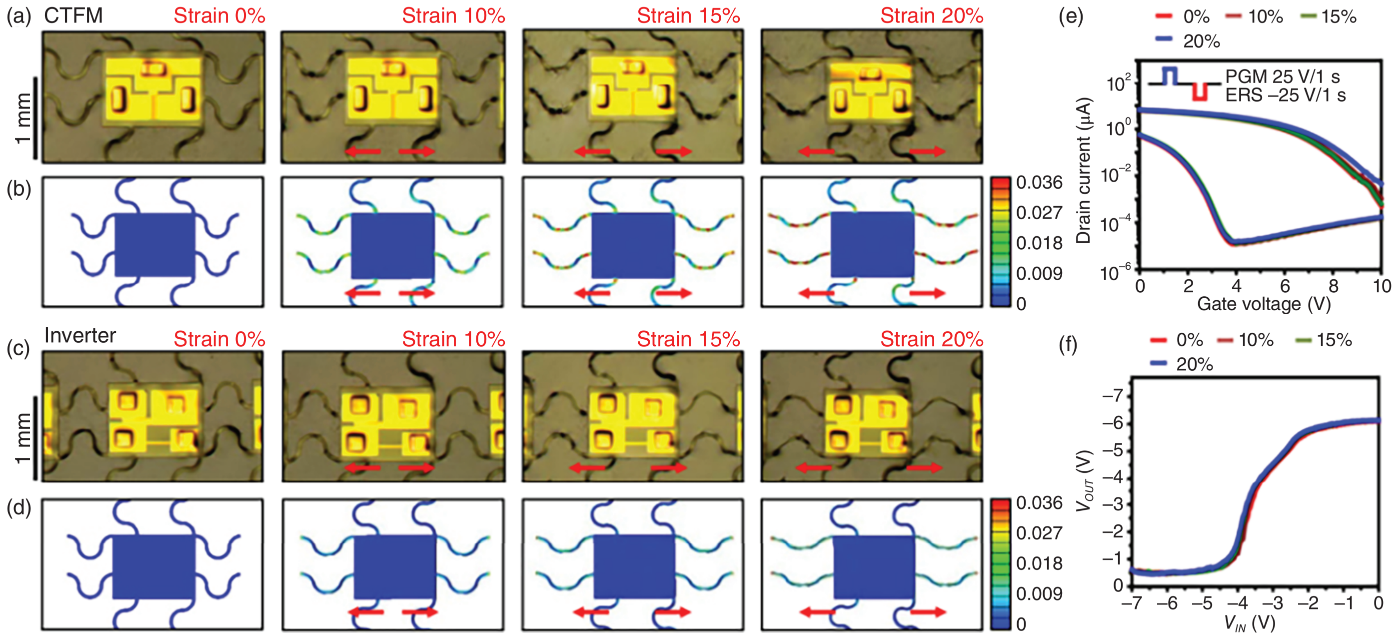

Figure 1.21 (a–f) Optical microscopic images and finite element analysis results of the serpentine interconnection inverter. Source: Son et al. [30]/with permission of American Chemical Society.

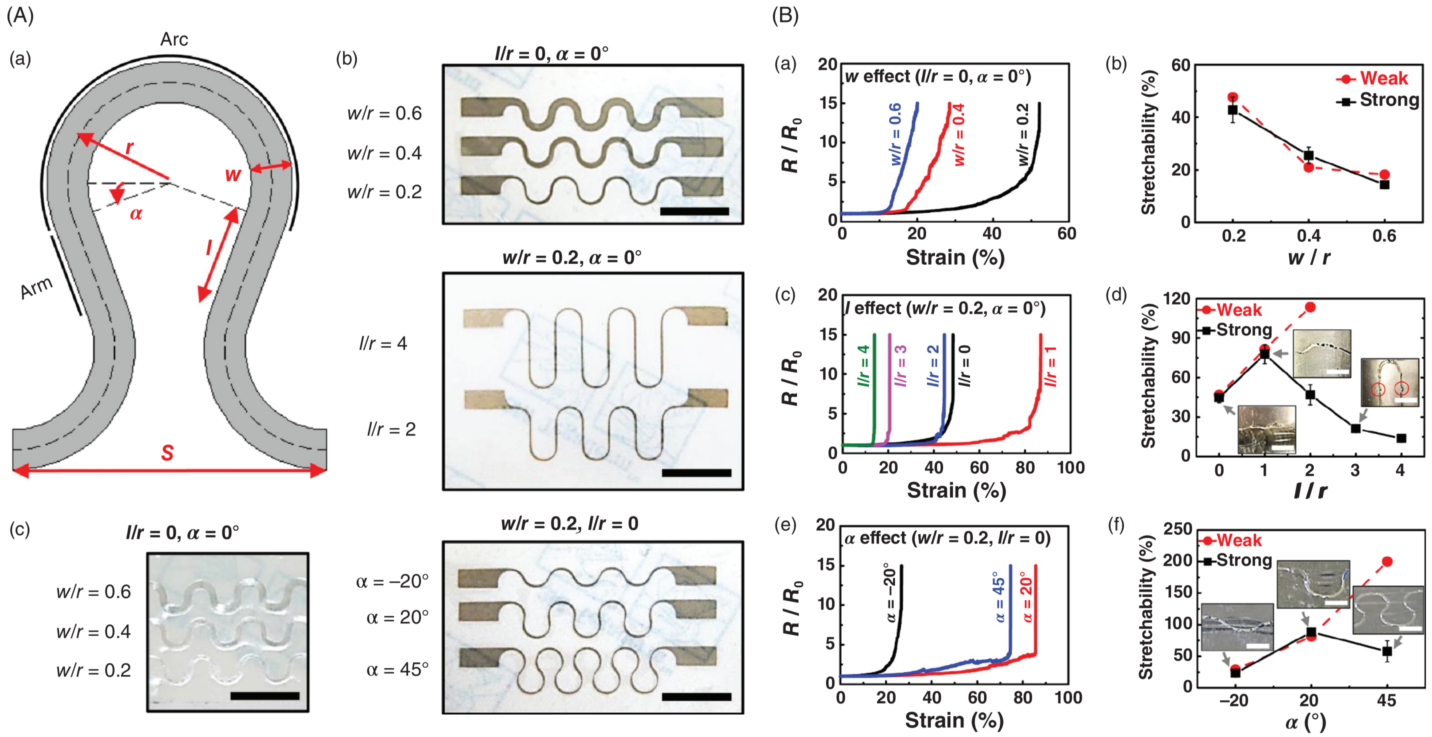

Figure 1.22 (A,B) Structure diagram of ITO serpentine tape and resistance-strain test results. Source: Yang et al. [31]/with permission of Elsevier.

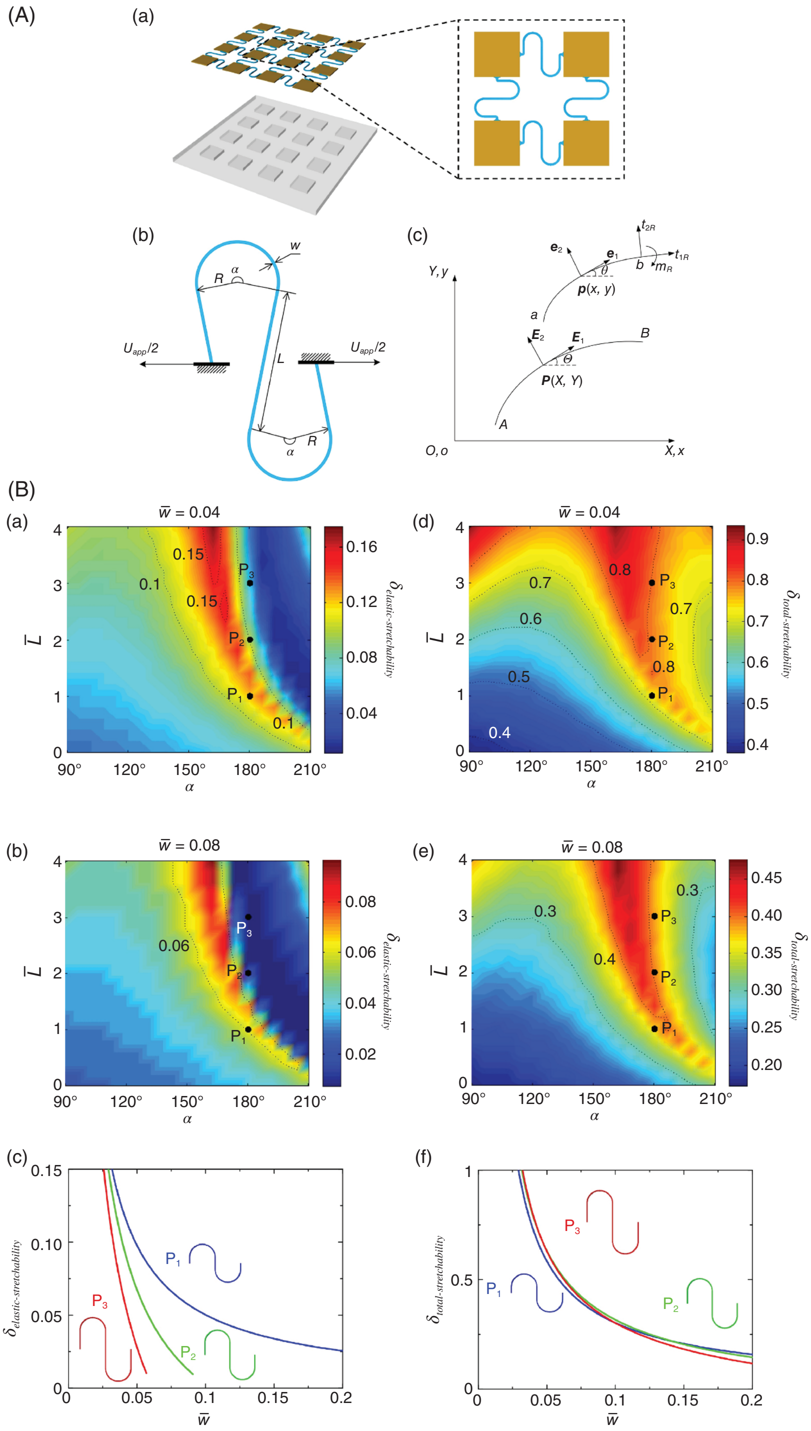

Figure 1.23 (A,B) Analytical model diagram and tensile results of the serpentine structure. Source: Fan et al. [32]/with permission of Elsevier.

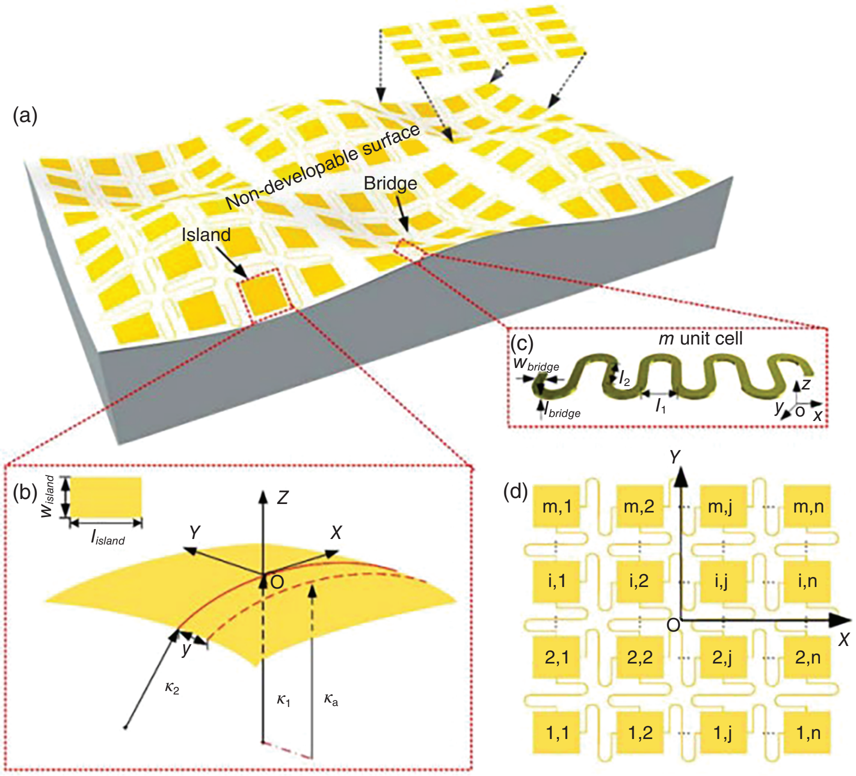

Figure 1.24 (a–d) Schematic diagram of island bridge structure on nondeployable surface. Source: Xiao et al. [33]/CC BY 4.0/MDPI.

substrates. Zhang et al. [35] studied the buckling physical properties of this stretchable suspended serpentine wire structure by analyzing the model, finite element calculation, and quantitative experiments and designed the serpentine layout of the super-stretchable electrode. The buckling initiation and post-buckling behavior are studied, and the scaling laws of critical buckling strain and elastic behavior limit are determined. Two buckling modes, symmetric and antisymmetric modes, are identified and analyzed. The experimental images and numerical results show that the relevant post-buckling processes are significantly consistent (Figure 1.26).

Zhang et al. [36] bonded the serpentine interconnect to the substrate and performed fracture tests on structures formed with and without pre-strain, quantitatively demonstrating the possible tensile enhancement effect. FEA illustrates the effects of various materials and geometric parameters. As the thickness of the metal increases, the elastic tensile properties decrease sharply, which is due to the change in the buckling mode. The experiment shows no wrinkling from the local wrinkling at the small thickness to the large thickness. An analytical model was created to quantitatively predict the wavelength of this wrinkling and explain the thickness dependence of the buckling behavior (Figure 1.27).

Su et al. [37] developed a different stretchable structural path in which the coarse rod geometry replaces the ribbon layout, resulting in scissor-like deformation rather

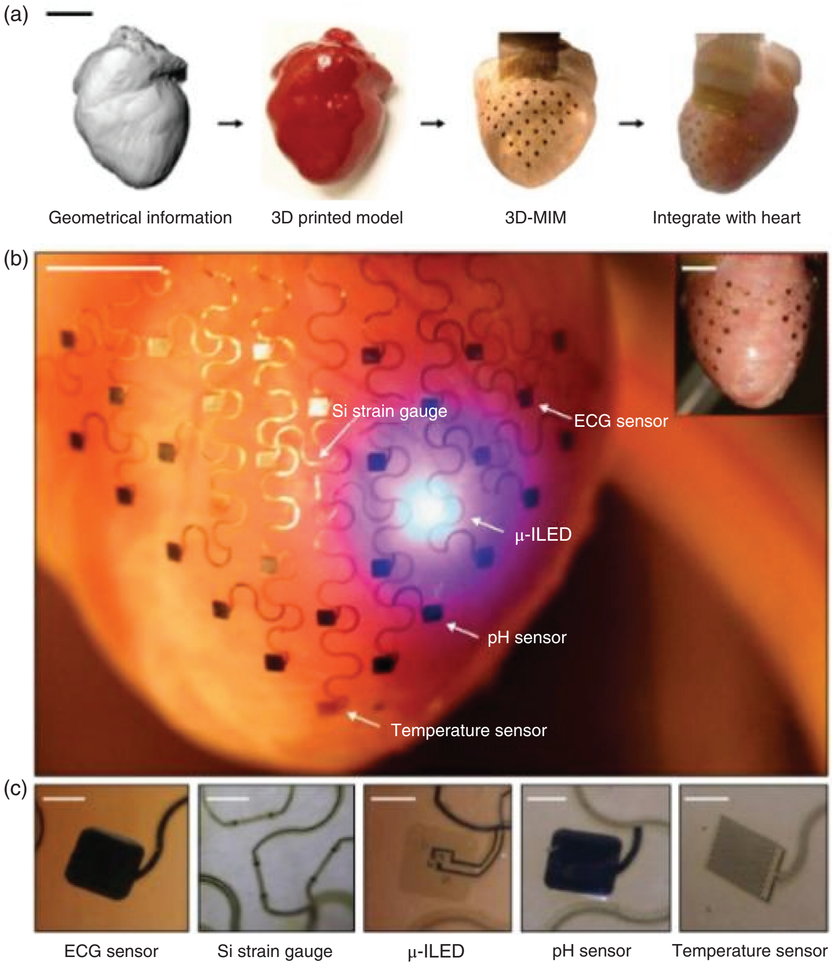

Figure 1.25 3D-MIMs are used for spatiotemporal measurement and stimulation of the epicardial surface. (a) Graphical description of critical steps in device design and manufacturing. (b) Langendorff perfusion of a representative 3D multifunctional capsule (3D-mim) image on the rabbit heart. (c) Amplification of functional elements in conformal contact with the epicardium. Source: Xu et al. [34]/with permission of Springer Nature.

than in-plane or out-of-plane buckling mode. The experimental and analytical models show that the metal and silicon structures with this rod-like structure can be stretched to 350% and 90% strain without fracture, respectively. Compared with previous studies, this is a significant improvement, achieving 54% stretchability in pure bent, narrow metal interconnects. The metal features of these layouts have additional advantages; they provide low resistance as interconnects to enhance operations in the examples, including high-power LED lights and solar cell arrays (Figures 1.28 and 1.29).

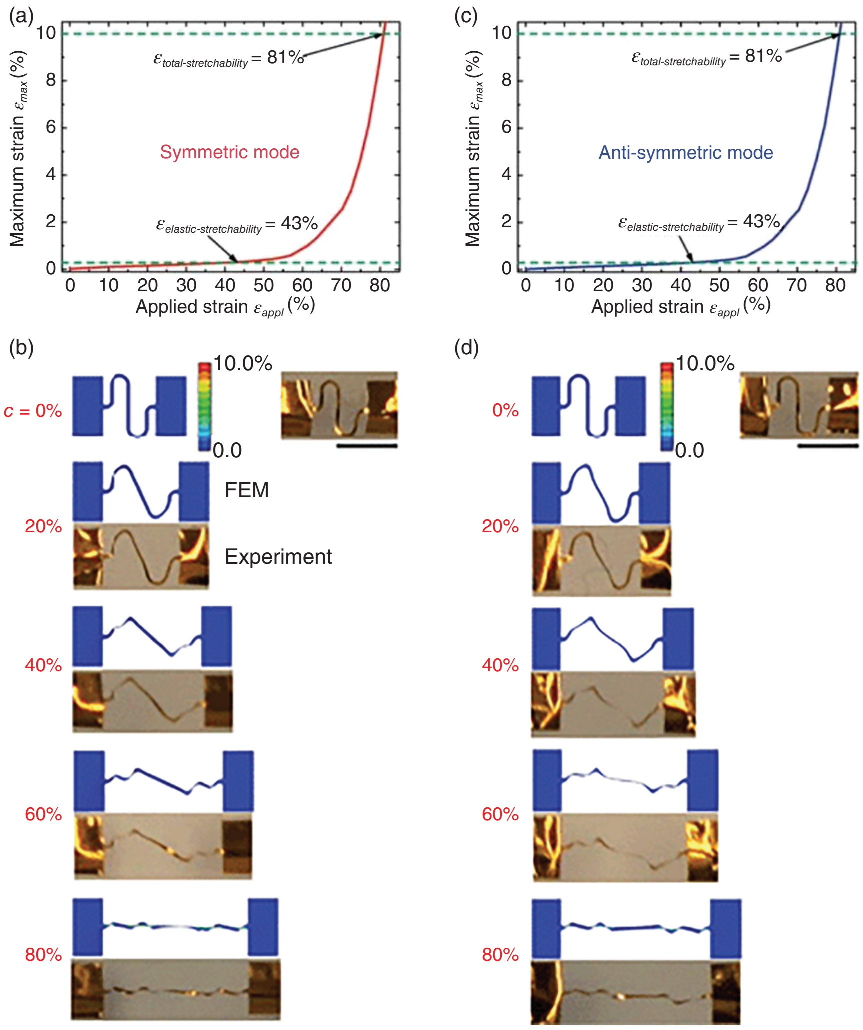

Figure 1.26 Experimental and numerical analysis of the buckling mechanism of serpentine conductors with a strain of 0–80%. Source: Zhang et al. [35]/with permission of Royal Society of Chemistry.

Pan et al. [38] studied the influence of the modulus and thickness of the elastic substrate on the tensile properties of the serpentine interconnect material. FEA shows that the elastic tensile properties significantly increase, and the substrate thickness is reduced. The low-cycle fatigue test confirms this trend by examining the tension required to form fatigue cracks associated with plastic deformation. To clarify the mechanical principle, the buckling behavior of deformed serpentine interconnections on substrates with different thicknesses was studied. Scanning electron microscopy and 3D optical profiler studies confirmed the transformation of buckling behavior. The overall buckling found in thin substrates can accommodate

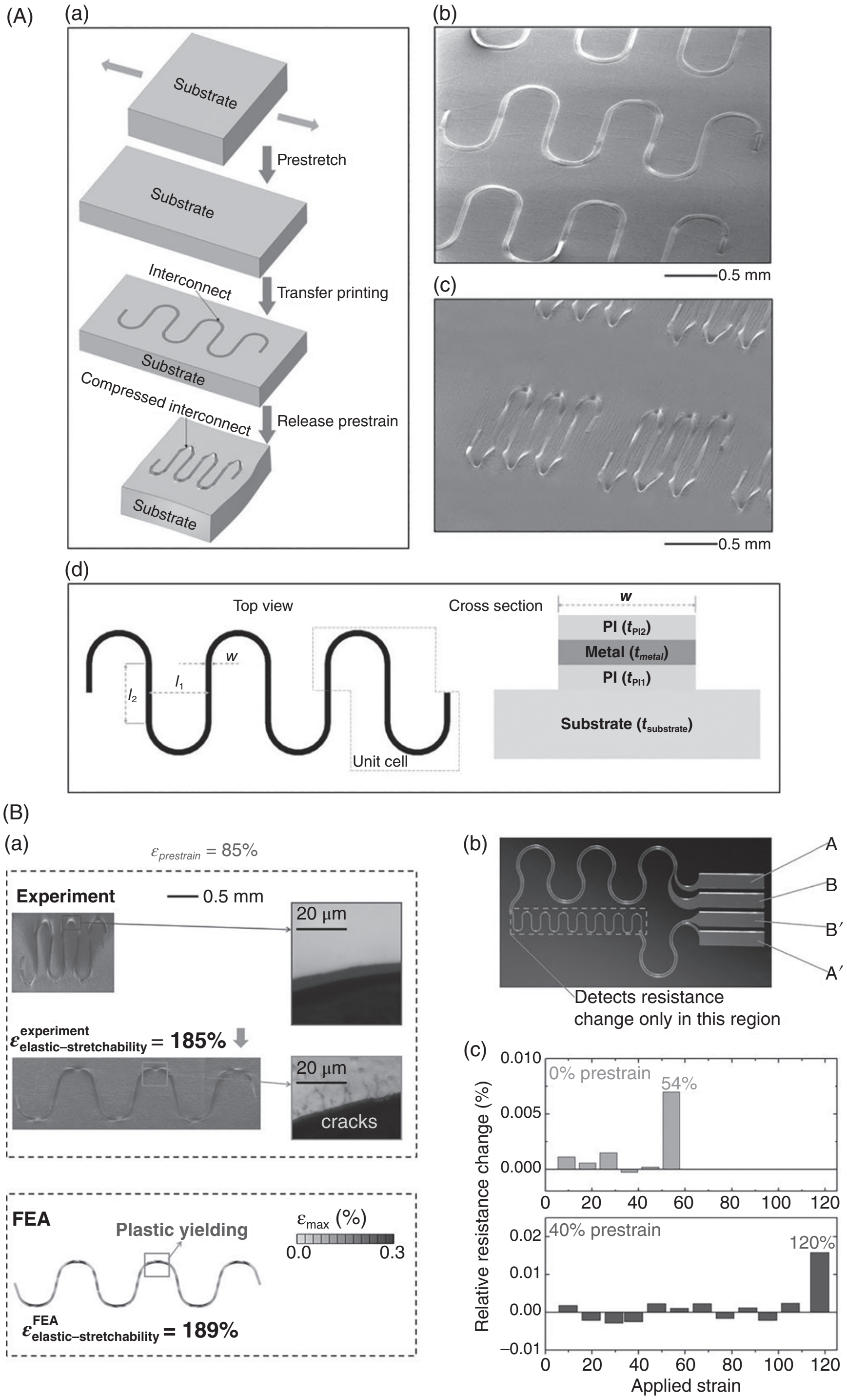

Figure 1.27 (A,B) Schematic diagram and tensile fracture of fully bonded serpentine wire. Source: Zhang et al. [36]/with permission of John Wiley & Sons.

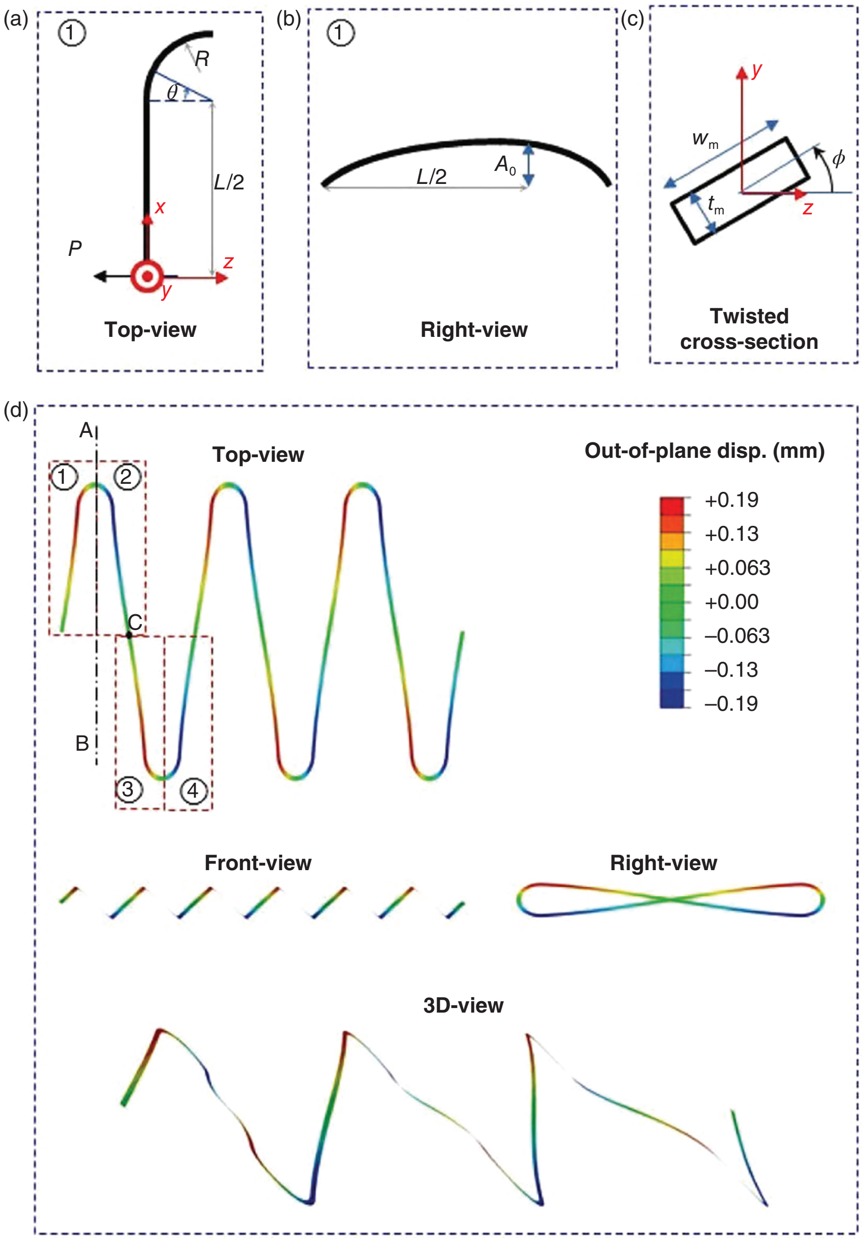

Figure 1.28 (a–d) Deformation mode of thick rod serpentine conductor under buckling state. Source: Su et al. [37]/with permission of John Wiley & Sons.

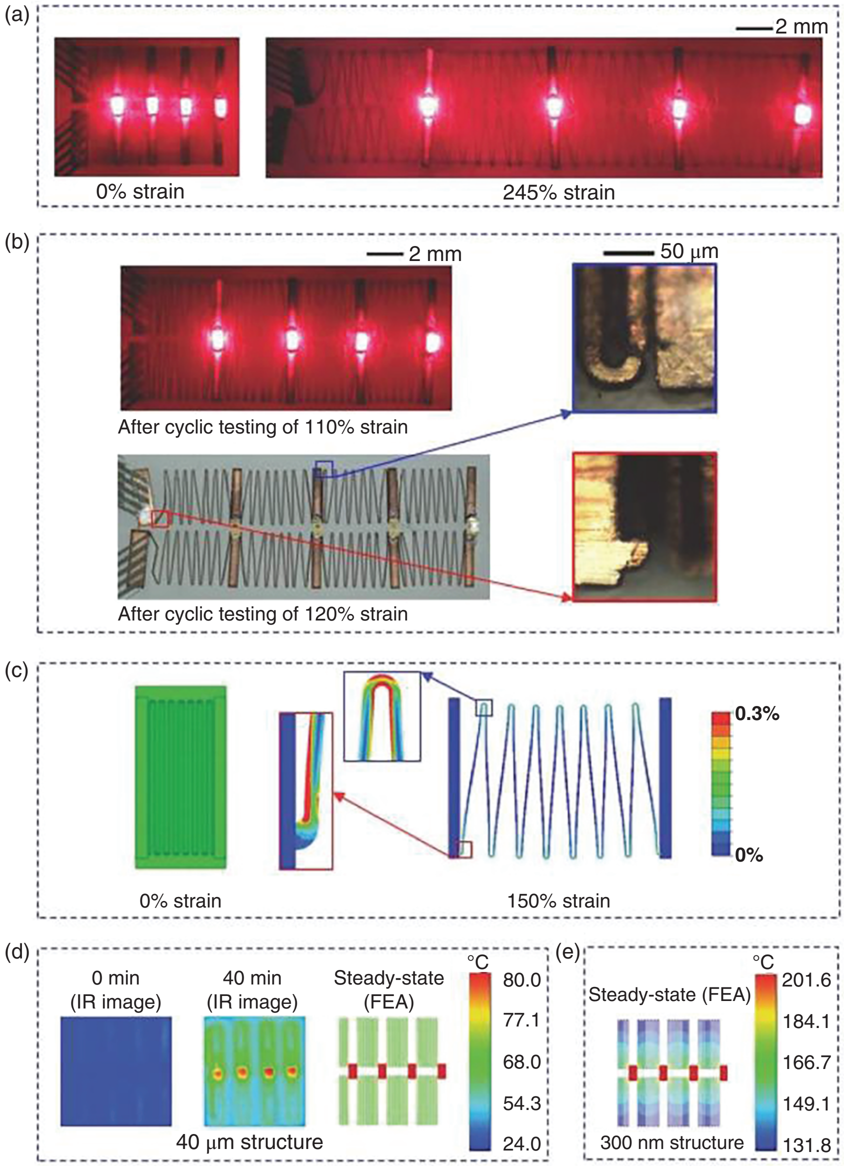

Figure 1.29 (a–d) Shear interconnection demonstration of thick rod serpentine wire in stretchable LED lamp array. Source: Su et al. [37]/with permission of John Wiley & Sons.

large stretches before the serpentine plastic deformation, which dramatically improves the stretchability of these systems (Figures 1.30 and 1.31).

1.1.4 2D Spiral Interconnects

With the more profound research in two-dimensional planar stretchable structures, a typical 2D spiral structure in nature has attracted much attention due

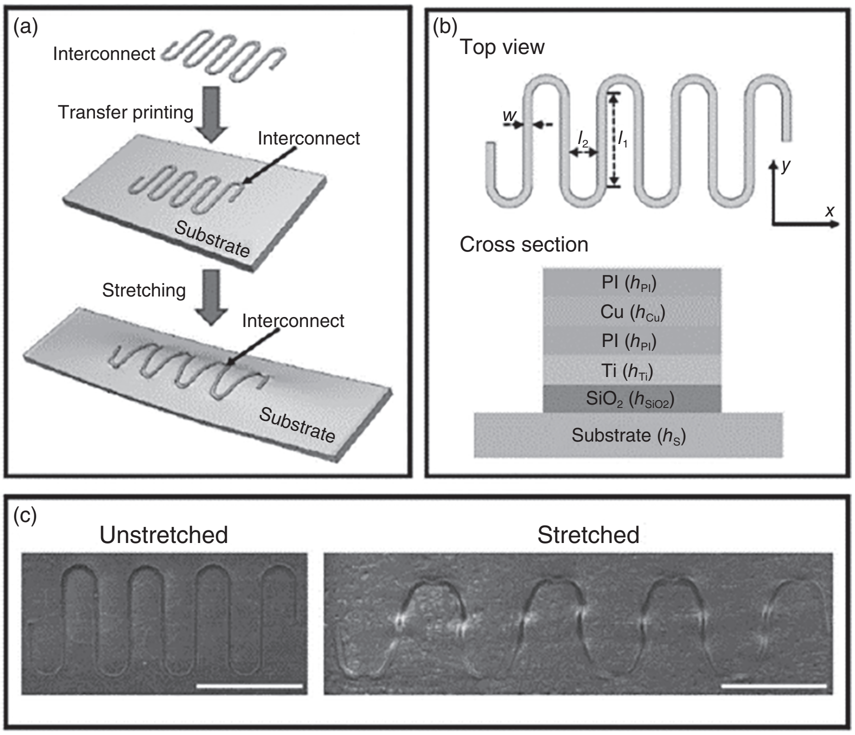

Figure 1.30 (a–c) Step diagram of manufacturing serpentine interconnect wire on soft substrate. Source: Pan et al. [38]/with permission of John Wiley & Sons.

to its excellent tensile properties. Compared with serpentine interconnects, the spiral-based interconnects can offer higher stretchability [39]. When the 2D spiral interconnect is subjected to transverse force, the spiral structure rotates around the circle's center to release the curly interconnect. The structure shows excellent tensile deformation on the macro level. Once the external force is removed, the strain energy of the structure is released, and the interconnect returns to its original position and shape. The mechanical principles of such structures as tape measures are very similar. They both have low elastic modulus (significant tensile rate) and high yield strength (elastic deformation capacity) properties. Therefore, the 2D spiral structure is highly matched with the mechanical behavior of flexible materials and has been widely used in flexible electronics.

Archimedes spiral is the most common 2D spiral structure in flexible electronics, and its slight curvature and uniform variation are very conducive to sizeable tensile deformation. Lv et al. [39] used Finite element analysis (FEM) to analyze three structures (serpentine, self-similar, and helical) tensile properties. Among the interconnects of the three structures shown in Figure 1.32, the Archimedean spiral structure has the largest elastic stretchability, reaching 200%. In contrast, the elastic stretchability of the periodic snake structure and the self-similar structure is only 112% and 90%, respectively. The out-of-plane deformation of the curly interconnects

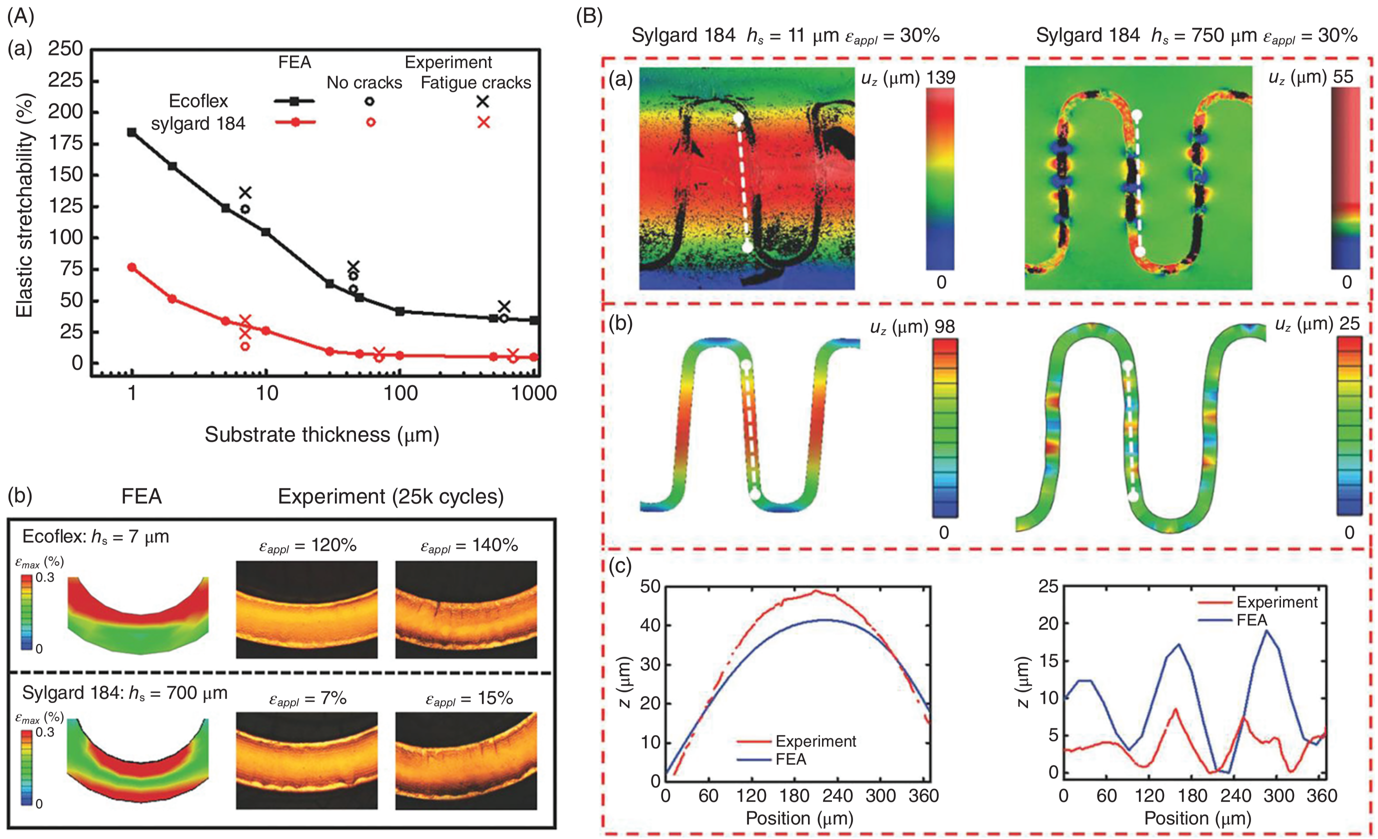

Figure 1.31 (A,B) The results of the tensile properties of serpentine wires varying with the thickness and modulus of the elastic substrate. Source: Pan et al. [38]/with permission of John Wiley & Sons.

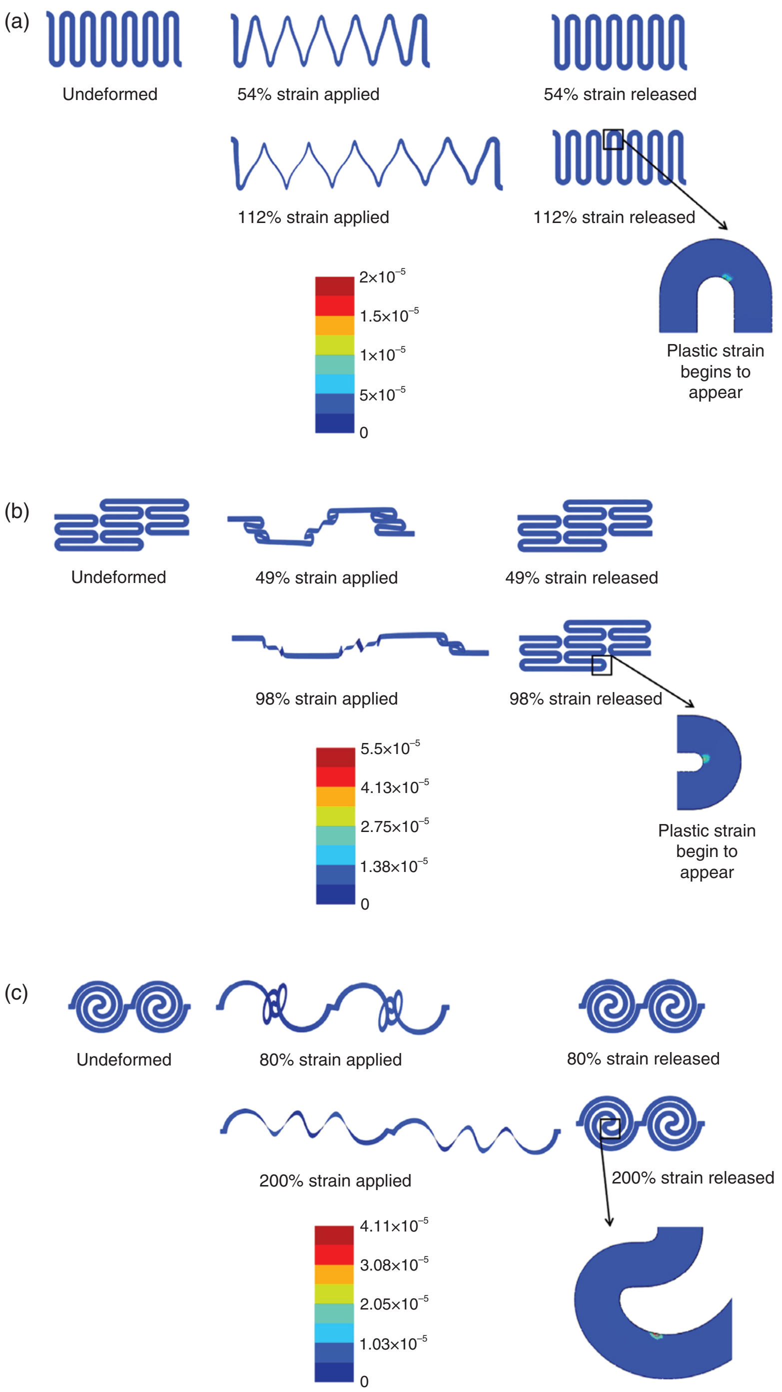

Figure 1.32 Stress distribution of serpentine, self-similar, and helical structures in plane. Source: Lv et al. [39]/with permission of Elsevier.

compensates for the in-plane tension. The structure only has some areas that have plastic deformation under large deformation. However, the plastic deformation in the limited area does not affect the overall elasticity. So, this structure can return to underformed shape after external unloading.

To further meet the unique requirements of different applications for spiral structures, Yuan and Wang [40] developed a theoretical model for the mechanical responses of Archimedean-spiral interconnects under the in-plane stretching based on the finite deformation plane-strain beam theory. As shown in Figure 1.33, the key parameters of the mechanical responses including the effective tensile stress, maximum strain, and deformed configurations are analytically derived and validated by FEA for a wide range of geometric variables.

The 2D spiral structure central has excellent stability. The 2D helix-node design proposed by Huang et al. [41] not only ensures the strain isolation of the node region but also limits the out-of-plane deformation of the spiral interconnect during the development process. The structure wraps 1.6 μm-thin silicon spiral bands around circular silicon islands (200 μm). The helix is pulled out under in-plane tensile load while the silicon island rotates around the circle's center. The force-displacement relationship of the structure obtained by FEM is shown in Figure 1.34. According to the above research results, the helix rotates around the center of the node in the plane under the in-plane tensile load, and the structure center is relatively static. Therefore, the interconnection of many islands-bridges adopts the Archimedean helix structure. Alcheikh et al. [43] studied the relationship between the tensile properties of island bridge structures and the geometric parameters of interconnects through mathematical modeling and experimental verification. As shown in Figure 1.34b, when the three interconnects reach 100% tensile rate, the Archimedean structure's maximum stress is the smallest, $\sigma_{\max} = 273\,\text{MPa}$, while the maximum stress of spiral structure and serpentine structure is 454 and 518 MPa, respectively. The results show that the Archimedes interconnect has the lowest stress and, thus, the highest ductility. Sung et al. [42] used the island bridge design to develop a large-area chip network using stretchable electroplated copper helical wires as interconnects and realized the conformal deformation of rigid functional devices and two-dimensional surfaces. As shown in Figure 1.34c, functional devices are directly integrated on nodes distributed in a two-dimensional chip network that are mechanically and electrically connected to surrounding nodes by stretchable copper interconnects. Interconnectors can expand the distance between functional devices by several orders of magnitude to build an extensive area chip network of interconnected devices. Figure 1.34d shows the SEM image of the Archimedes' interconnect with copper plating on a silicon substrate.

The helix structure achieves a large in-plane tensile ratio due to the spiral folding around the circle's center, but the helix itself is not designed to be stretchable. The tensile ratio of the structure reaches the limit after the helix is completely pulled out [44]. To further explore the tensile properties of 2D spiral structures, Rehman and Rojas [45] further optimized the design of 2D spiral interconnects and added a serpentine structure to the interconnects to improve the tensile properties, as shown in Figure 1.35a,b. The structure considers the integrated design of a double-arm

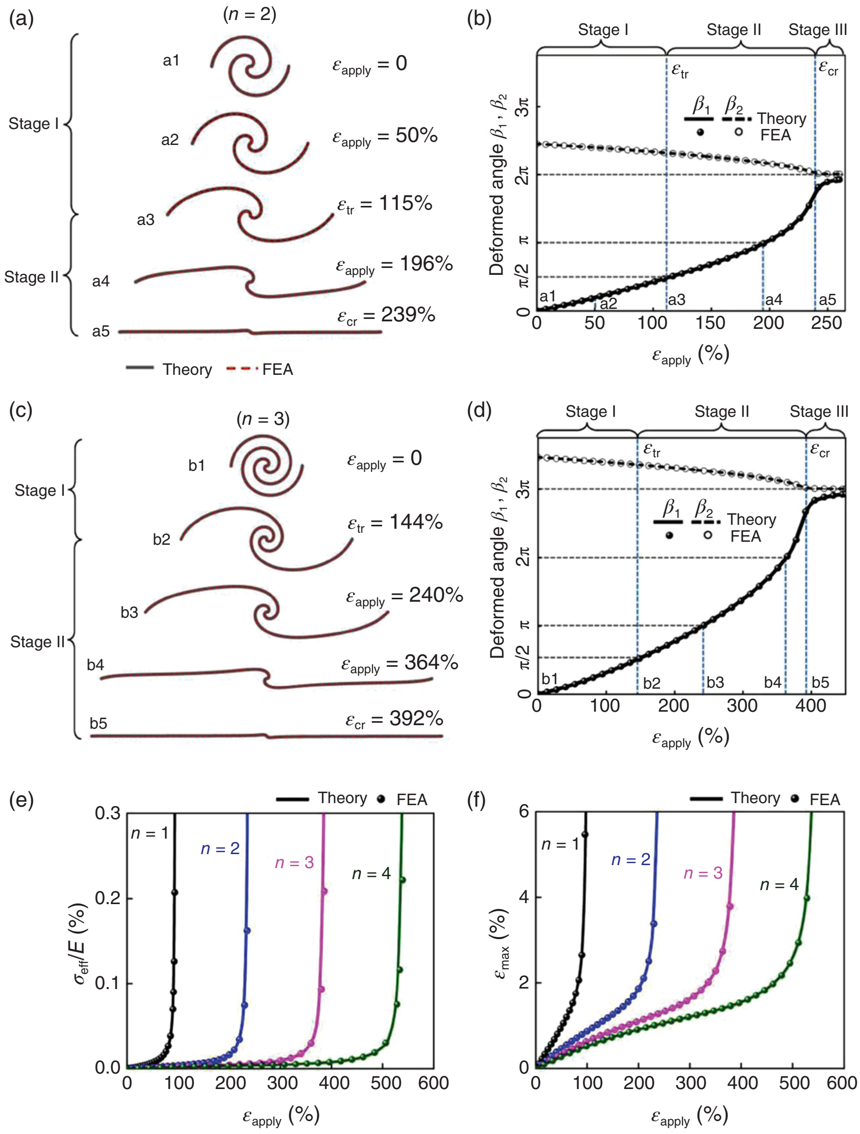

Figure 1.33 (a–f) The deformation and mechanical responses of the Archimedean-spiral interconnect. Source: Yuan and Wang [40]/with permission of Elsevier.

helix with serpentine and horseshoe structural variants, and its mechanical response under applied deformation is analyzed by FEA. As shown in Figure 1.35e,f, the proposed composite structure provides excellent tensile capacity compared to the original, unoptimized helical structure. It shows a 55% reduction in stress/strain, as well as a uniform distribution of stress/strain changes. The maximum stress of the optimized composite spiral structure is reduced to 1779 MPa, which is 58.47% lower than that of the original spiral structure.

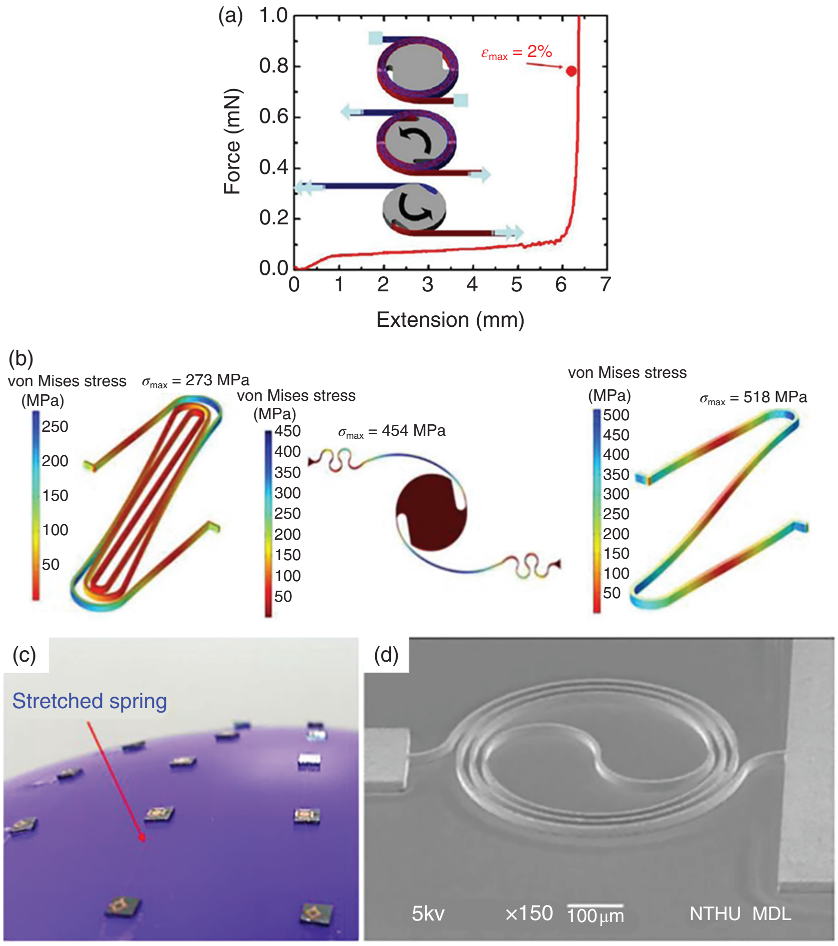

Figure 1.34 Mechanical properties and applications of 2D helical-node interconnect designs. Source: Sung et al. [42]/with permission of IOP Publishing.

1.1.5 3D Spiral Interconnects

Flexible electronic devices have pursued more excellent stretchability and stronger mechanical robustness. To further improve the device's performance, the researchers broke through the 2D plane to conduct in-depth research on the 3D interconnect structure. As a highly innovative design in stretchable electronics, the 3D helix interconnect provides structures with extremely high elastic stretchability and mechanical stability, it is an ideal platform for flexible wearable devices.

The 3D interconnection structure is the spatial extension of the 2D structure. Huang's group [46, 47] proposed a strategy to transform 2D structure geometry into 3D structure through compression buckling and designed and verified more than 40 representative 3D interconnected structures by combining theoretical analysis, FEA, and experiments. This novel geometric transformation strategy is based on the

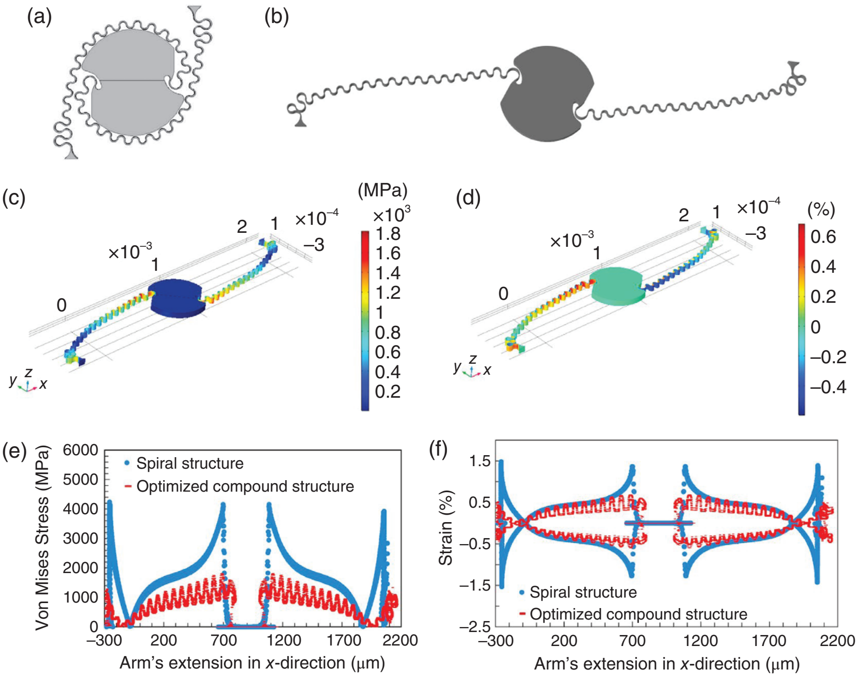

Figure 1.35 The influence of interconnecting serpentine structure on tensile properties. Source: Rehman and Rojas [45]/with permission of Elsevier.

theory of minimizing the total strain energy of the system after the 2D structure is spatially deformed. The 2D filamentous precursors of different shapes form covalent bonds with the in-plane pre-stretched elastomer through predefined bonding sites to achieve the transfer on the elastic substrate. When the pre-stretched substrate strain is released, the 2D filament precursor is subjected to in-plane pressure, triggering both in-plane and out-of-plane translational/rotational motion and bending/torsional deformation in the nonbonded region simultaneously. Finally, the 3D structure achieves the balance between the adhesive force of the substrate and the strain energy of the bent and twisted strips, forming a stable 3D helical structure.

There are a variety of 3D spiral interconnect structures, each of which has particular mechanical behavior, and researchers can design structures according to application requirements. Xu designed a variety of helical structures using FEA and experiments. By modifying the structure of 2D precursors and changing the distribution of bonding sites, structures such as double helix, nested coaxial helix, helix with opposite chirality, and anti-helix were obtained. To study the mechanical behavior of different 3D spiral interconnected wires, Yan et al. [47] selected the process design with FEA as the guide and realized that the maximum strain in the 3D structure was limited to far lower than the fracture threshold of the component materials, which significantly improved the yield of the produced good products. Based on the principle of minimization of total strain energy caused by different forms of spatially correlated deformation, Liu et al. [48] proposed an analytical

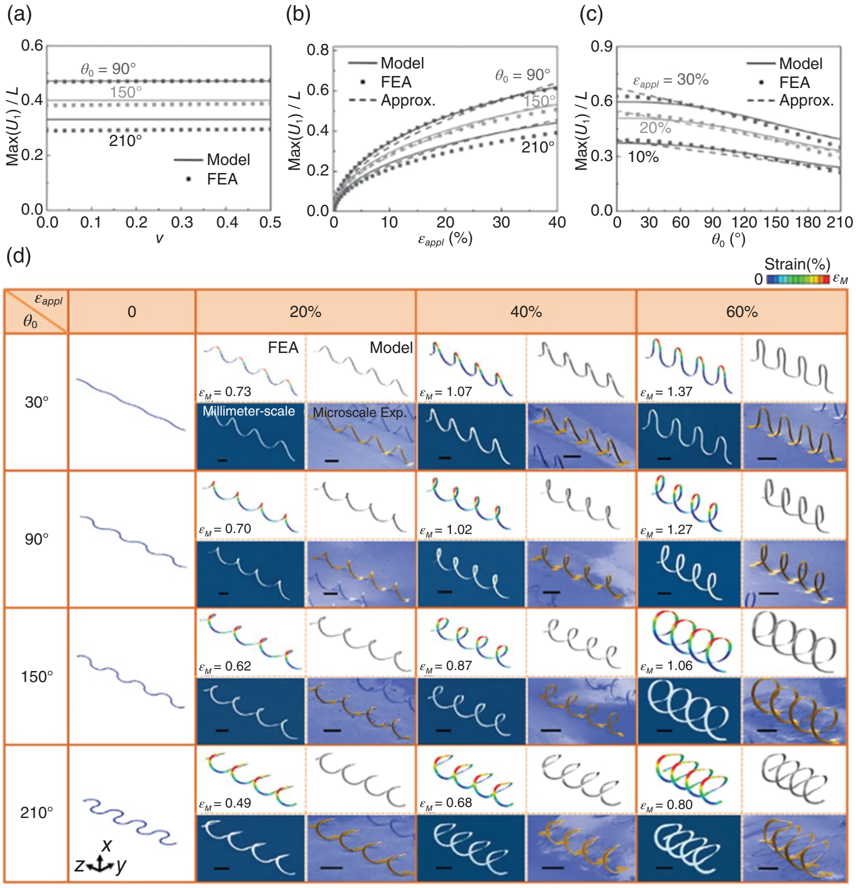

Figure 1.36 Various 3D spiral interconnect structures and mechanical properties. Source: Liu et al. [48]/with permission of John Wiley & Sons.

model of compression buckling of serpentine microstructure. Through FEA and theoretical analysis at the micron-millimeter scale, the theory reveals the general scaling laws of three manufacturing parameters (related to loading, material, and two-dimensional geometry) in Figure 1.36a–c.

Using the analytical solution to select various design parameters can avoid brittle fracture or plastic yield of the structure during assembly. As shown in Figure 1.36d, under different compressive strain levels (0%, 20%, 40%, 60%), the torsion degree of the 3D spiral structure increases significantly as the arc angle increases from 30° to 210°.

3D structures have unique packaging methods. Different from the traditional 2D structure, mechanical deformation generally occurs in the in-plane [49–51], and the out-of-plane packaging layer has little influence on the mechanical properties of the structure. In contrast, the out-of-plane packaging strategy of the 3D structure seriously affects the device's performance. A reliable solution for encapsulating

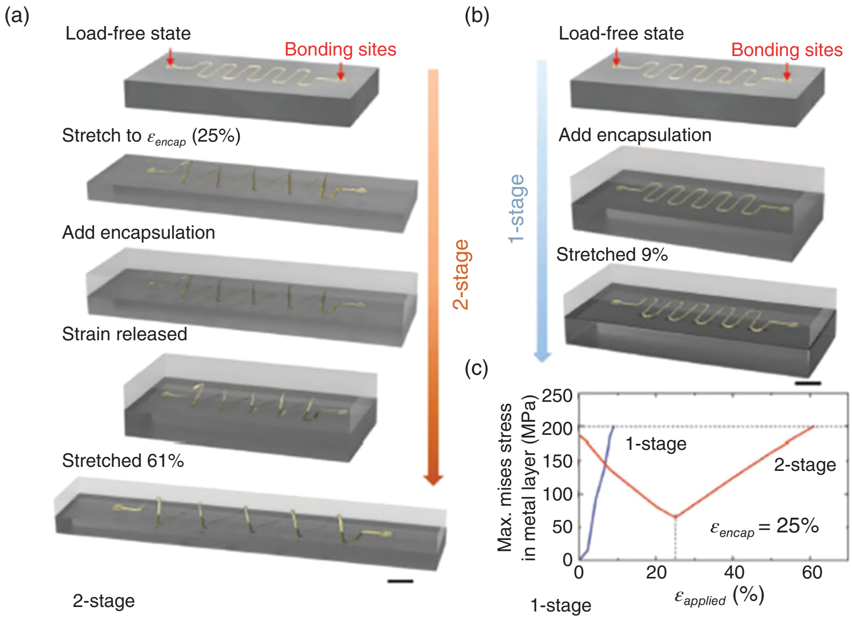

Figure 1.37 (a–c) 3D interconnects' soft packaging strategy. Source: Li et al. [49]/with permission of John Wiley & Sons.

scalable electronic platforms is critical for practical applications, and developing a universal solid packaging strategy that does not sacrifice stretchability remains a challenge. Reliable packaging methods hinder the application of 3D spiral interconnected structures. Therefore, Li [49] proposes a soft packaging strategy that can be broadly applied to various stretchable interconnect designs, the so-called "two-stage soft encapsulation" strategy. This strategy enables reliable packaging of (2D) serpentine structures, 2D fractal structures, and 3D spiral structures. Different from the traditional nonload packaging strategy, this strategy forms a solid package when the electronic system is in the pre-stretch state and releases the pre-stretch after the completion of the packaging process. In this way, the constraints of solid encapsulation on interconnect deformation under external loads can be mostly alleviated, as demonstrated by experiments and mechanical modeling. As shown in Figure 1.37, using FEA quantitative study illustrates an optimized two-stage packaging process that can maximize the stretchability of flexible devices.

1.1.6 2D Fractal Structure

Unlike other flexible electronic products, the sensing elements in wearable devices require a more significant stretch rate but also need to cover a large area of the sensing object, which is not available in traditional interconnects. The fractal interconnect structure solves this problem effectively. Fan et al. [52] first proposed the fractal design concept of stretchable electronic devices. Figure 1.38 shows the interconnect design of six different fractal structures. The interconnects are wholly bonded on the

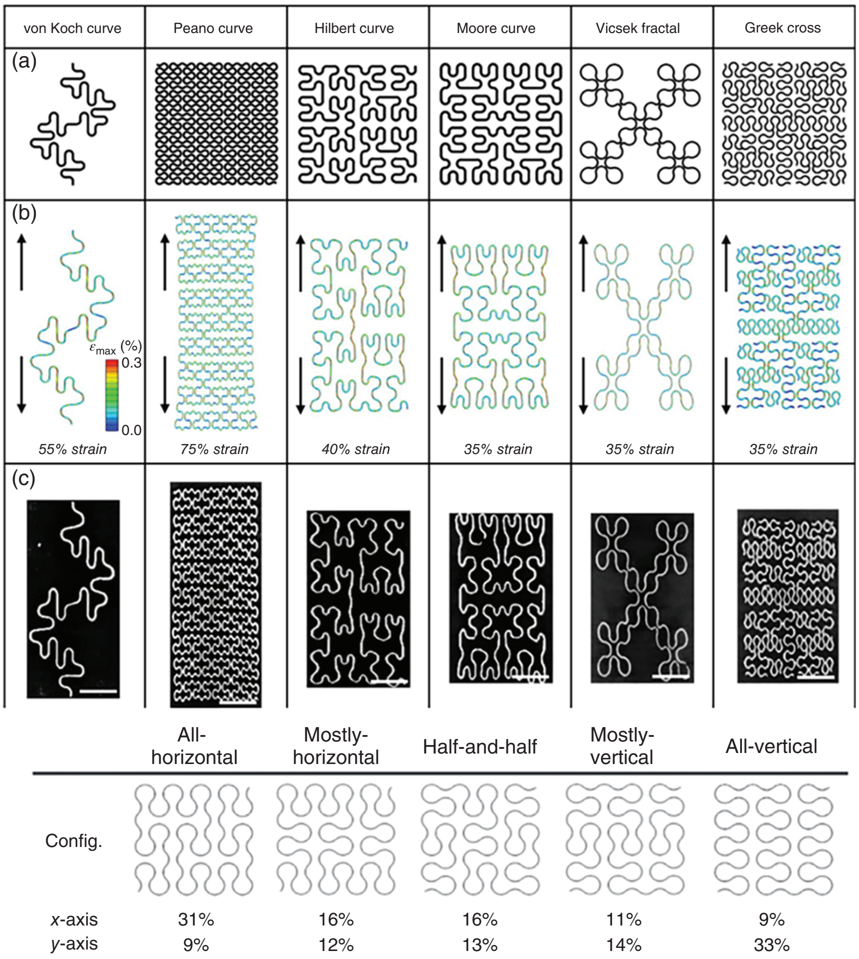

Figure 1.38 (a–c) Interconnect structural performance of 2D fractal structures and second-order Peano layout. Source: Fan et al. [52]/with permission of Springer Nature.

elastic substrate to form a tensile structure. The deformation results of the tensile structure under uniaxial tensile load obtained by FEA and experimental methods are highly consistent, which verifies the reliability of the fractal interconnect design. To further investigate the tensile rates of fractal structures in different directions, Figure 1.38 shows the tensile rates in different directions when the interconnects of five different second-order Peano configurations reach the maximum principal strain ($\varepsilon_{\text{max}} = 0.3\%$). Even the same fractal structure of the same order has different layout methods, and the corresponding tensile properties are very different. Therefore, 2D fractal interconnection structure has a broad application prospect.

To realize the parametric design of 2D fractal structures, the researchers have studied the mechanical behavior of fractal interconnects, from the tensile deformation process of different order interconnects to the hierarchical calculation

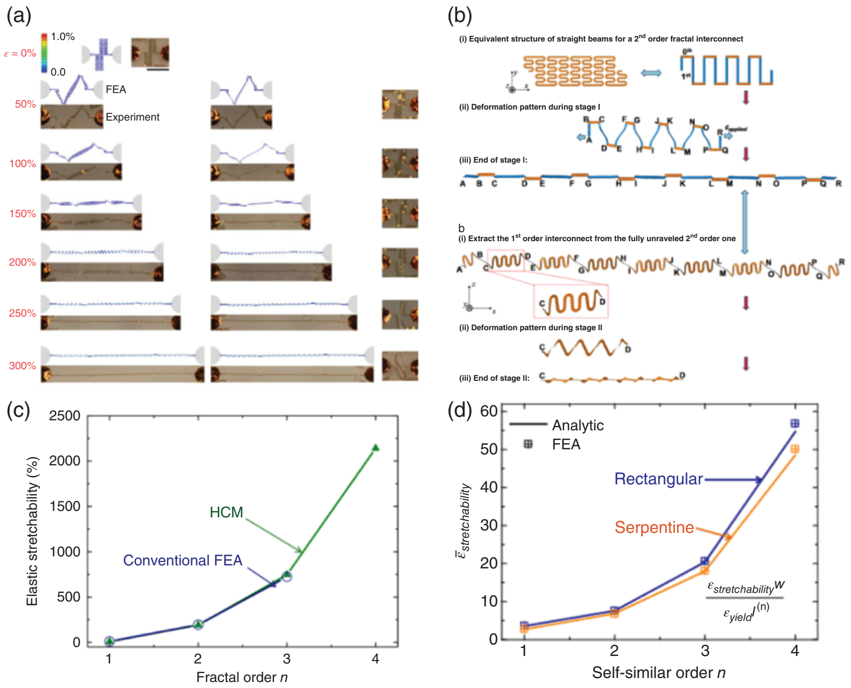

Figure 1.39 2D fractal structure expansion process and calculation results of hierarchical calculation model. Source: Zhang et al. [54]/with permission of Elsevier.

method, and established analytical, FEA models and experiments. Figure 1.39a shows the experimental and simulation study of buckling behavior in self-similar seek-arranged interconnects [53]. In transverse stretching, the second- and first-order structures are developed successively in stages. In the first stage, the secondary structure develops while the first-order structure does not deform. When the structural strain reaches 150%, the second-order structure unfolds entirely, and the deformation enters the second stage. The first-order structure begins to unfold, and this process continues until the maximum stretchability (≈300%) is reached. Based on the orderly unfolding of fractal structures, Zhang et al. [54] designed a fractal-inspired hierarchical computing model (HCM) for stretchable interconnects. The model is used for post-buckling analysis of fractal-inspired interconnects under tensile load. As shown in Figure 1.39b, these lower-order structures can be modeled as straight beams with adequate tension, bending, and torsion flexibilities. Once the highest (n) order structure is sufficiently stretched, the ($n - 1$) order structure begins to disintegrate, but the ($n - 2$) order and lower order structures remain intact and can be modeled as beams. This process continues until the first-order structure disintegrates and finally reaches the total stretchability. Figure 1.39c uses FEA and HCM to calculate the stretchability of the structure under different fractal orders. As the fractal order increases from 1 to 4, the elastic stretchability can be increased by 200 times.

Based on the sound theoretical model and FEA results, Zhang et al. [55] established recurrence formulas for different self-similar orders. The analytical solutions in Figure 1.39d agree well with the FEA results, both of which indicate that the elastic ductility of self-similar structures can be more than doubled when the order is doubled. For systems with surface filling rates of 50% and 70% of active devices, the design optimization results in elastic stretchability of 90% and 50%, respectively.

Due to the highly complex and diverse microstructure inherent in higher-order fractal patterns, fractal structures often undergo complex, nonlinear deformation under mechanical loads. The intrinsic relationship between nonlinear mechanical response and microstructure geometry is essential in practical applications. Ma and Zhang [56] studied the nonlinear stress-strain curves and elastic tensile properties of a class of fractal horseshoe microstructures based on the theoretical model of the ordered development mechanism. Analytic solutions were obtained for some key mechanical quantities, such as the elastic modulus and the tangent modulus at the beginning of each deformation stage. Both the FEA and experiments were carried out to validate the model. Systematic analyses of the microstructure–property relationship dictate how to leverage the various geometric parameters to tune the multistage, J-shaped stress–strain curves.

Perfect mechanical analysis has laid a solid theoretical foundation for applying fractal structure in flexible electronics, and more and more flexible electronic devices are used in fractal structure design. Xu et al. [57] used a fractal electrode array distributed on the periphery of the rabbit heart to provide a direct interface on the epicardium for spatiotemporal programmed electrical stimulation. Norton et al. [58] designed a flexible brain-computer interface system based on the Peano curve to form a self-similar design with spatial changes by using the soft and stretchable characteristics of the fractal network electrode, which can be installed on the auricle and other complex topological surface structures of the human body for a long time. Further, Kim et al. [59] designed and developed a set of electronic skin based on fractal structure. The sensor not only has more excellent stretchability but also has superior performance of extensive detection range and high spatial and temporal resolution. In addition, the flexible electronics of fractal structures are also used in clinical medicine. In Figure 1.40a, Hattori et al. [60] designed a multifunctional skin-like electronic device for quantitative clinical monitoring of skin wound healing. The device packages Peano fractal pattern wires in PI to form a multilayer structure that can maintain a stable response at 30% uniaxial stretching, multimodal folding, biaxial stretching plus torsion, and 720° torsion. Figure 1.40b shows that the microscale X-ray coherence tomography (micro-CT) fractal structure of the device ADAPTS to mechanical strain levels that exceed the maximum (≈30%) generally experienced by the skin during biaxial, radial stretching.

1.2 Structural Design of Substrate

Flexible substrates are an essential component of stretchable inorganic electronics, unlike traditional electronics. Much research has focused on the design of flexible

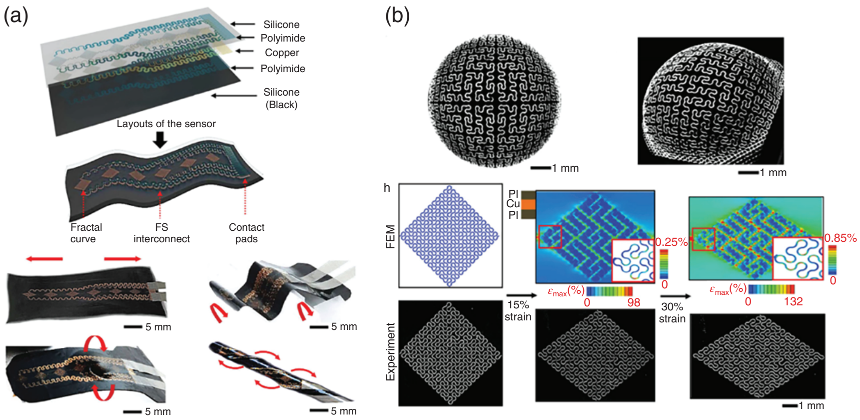

Figure 1.40 Conformal attachment of Peano curve electrodes to a flexible BCI system. Source: Hattori et al. [60]/with permission of John Wiley & Sons.

substrates to provide specific application platforms for flexible electronics. In this section, we focus on some representative substrate structure designs, including surface structure design, honeycomb substrate design, and curved substrate design.

1.2.1 Surface Structure Designs

In island interconnect designs, interconnects reduce area coverage, which is an urgent problem for many critical applications that require high area coverage, especially optoelectronic devices such as solar cells and photodetectors. By minimizing interfacial stresses between the device island and the substrate, it can achieve strain isolation of electronic devices from substrate deformation and provide desirable levels of stretchability with relatively large area coverage. Furthermore, additional optimization of island shape and layout can further improve stretchability and adequate area coverage [61]. Notched islands on thin elastomer substrates can serve as platforms for dual-junction GaInP/GaAs solar cells with microsized and ultrathin forms for stretchable photovoltaic modules [62].

In the field of flexible electronics, it requires different modes of mechanical deformation and achieves low complexity in the manufacturing process. Therefore, mesa-shaped elastomeric substrates supporting thin-film transistors (TFTs) and logic circuits (inverters) are fabricated using high-relief structures. The high-relief system is designed to minimize the strain experienced by the electronics, which are manufactured directly onto the pillar surface. In this design configuration, amorphous indium gallium zinc oxide-based devices can withstand different deformation modes. Bending, tensile, and torsion experiments with a radius of 6 mm, 20% uniaxial strain, and 180° torsion showed stable electrical properties [63].

In addition to the role of strain isolation, the integration of deformable serpentine interconnects, and inorganic functional materials with soft elastomeric substrates enables electronic devices to be deformed into any desired shape. Traditionally, serpentine interconnects are bonded to planar substrates, which limits the out-of-plane buckling of the serpentine interconnects and, thus, their stretchability. An integrated system that combines a serpentine interconnect with a toothed substrate can release part of the serpentine interconnect from the substrate. The advantage of this integrated system is its superior stretchability compared to serpentine interconnects on conventional planar substrates. Furthermore, this effect is predictable and within acceptable limits [64].

Tripod designs are another surface structure that can reduce strain in stretchable inorganic electronic systems. The substrate with a tripod structure enables the stretchability of the device without sacrificing its electrical properties, such as high area coverage of LEDs/photovoltaics/batteries/supercapacitors. Meanwhile, a base plate with a tripod surface relief structure allows the wrinkled installation to be suspended from the soft tripod base. This minimizes the contact area between the device and the deformed substrate, thereby significantly reducing the stress-strain at the interface [65]. As with the corrugated design, the structure can be fabricated by transferring a thin film on a prestrained substrate with a tripod structure. This design could be applied to many thin-film devices, such as electrodes in biointegrated electronics and graphene microstrips in microscopic supercapacitors. Rationally designed sinusoidal gold nanoribbons were fabricated into stretchable electrodes, and after 10,000 cyclic stretching/relaxation processes, they showed no noticeable resistance change under large deformation. Highly stretchable microsupercapacitors with stable electrochemical performance rely on the suspended wave-like structure of graphene microribbons, which reduces strain concentration in the electrode fingers and avoids shedding and cracking of the electrode material [66].

1.2.2 Cellular Substrate Designs

Figure 1.41 presents a thin stretchable ion sensor array for mounting on an open cellular substrate to facilitate solution exchange for biointegrated electronics. Fluid permeability on the sensor minimizes cumulative artifacts caused by the impermeability of traditional substrates. The experimental measurements and theoretical simulations in Figure 1.42 show that the morphologies obtained from FEA agree with the experiments. The pores in the cellular substrate did not limit

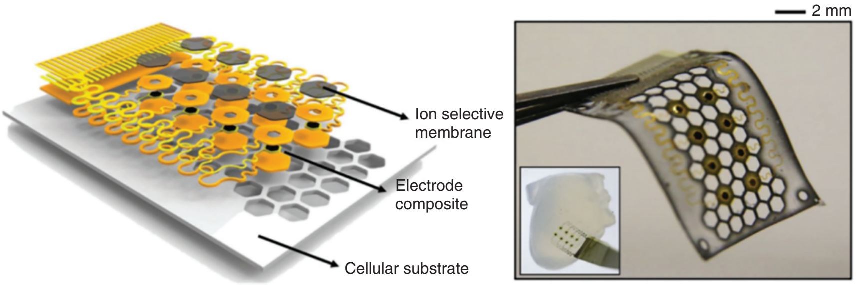

Figure 1.41 Schematic diagram and optical image of thin stretchable example sensor array design. Source: Lee et al. [67]/with permission of John Wiley & Sons.

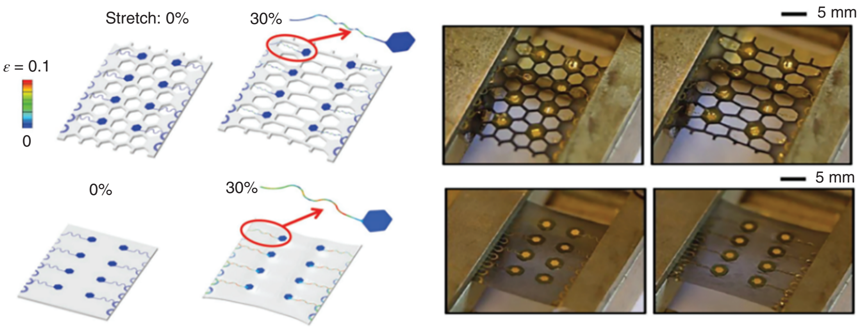

Figure 1.42 FEA results and optical images of ion sensors integrated on honeycomb (top) and solid substrate (bottom) under 30% uniaxial stretching. Source: Lee et al. [67]/with permission of John Wiley & Sons.

the buckling of the serpentine interconnect under 30% stretching. Compared to the solid substrate, the maximum strain of Au in the cellular substrate was reduced from 12% to 1%, significantly improving its stretchability.

In addition, the existing analytical constitutive models are primarily suitable for stretching along the direction of the cell wall [67]. Chen et al. [68] established an analytical constitutive model of the equivalent medium of cellular substrates under finite deformation. Figure 1.43 is a schematic diagram of the finite deformation mechanical model of a cellular substrate. The results show that the elastic stretchability of serpentine interconnects bonded to this equivalent medium represents a lower bound estimate for the case of actual honeycomb substrates, where the bonding adopts different alignments and positions. It provides a simple, conservative estimate of stretchability and has general engineering design rules for platforms utilizing cellular substrates in stretchable electronics. Zhu et al. [69] established an analytical constitutive model of the anisotropic equivalent medium of a cellular substrate under finite stretching in any direction. When the strain is <10%, the stress-strain curves in different tensile directions are the same. However,

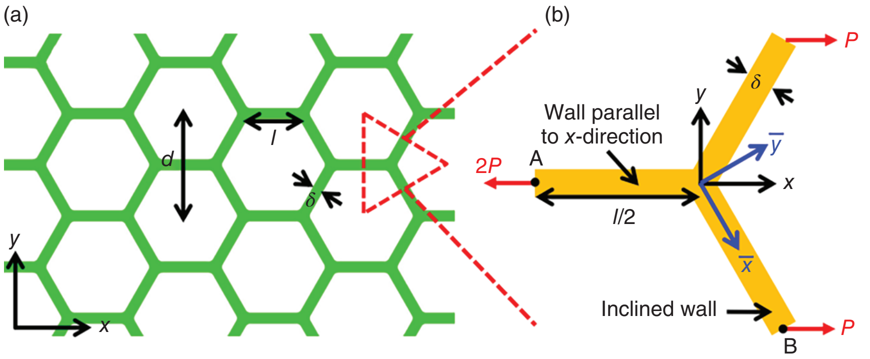

Figure 1.43 (a) Schematic diagram of the cellular substrate; (b) Mechanical model of the basic unit. Source: Chen et al. [68]/with permission of Elsevier.

as the stress increases, the stress-strain angles are significantly different, showing deformation-induced anisotropy. Comparing the results of linear and nonlinear elastic cell walls, the nonlinear stress-strain curve of Cellular substrates is mainly due to the limited rotation of the cell wall.

In biological integration applications, the mechanical properties of thin substrates can be adjusted by customizing the microstructure geometry to match the geometric shape of tissues or skin, resulting in improved biocompatibility and conformability. Hard and soft structural composites discovered in biology inspire the design of advanced synthetic materials. Jang et al. [70] introduced a deterministic approach to stress-/strain-responsive low-modulus thin film materials that can be precisely tailored to match the nonlinear properties of biological tissues, with applications ranging from soft biomedical devices to tissue engineering structures. This approach combines a low-modulus matrix with an open stretchable network as a structural reinforcement, producing composites with various desired mechanical responses, including anisotropic, spatially heterogeneous, hierarchical, and self-similar designs. Figure 1.44 shows an image of a uniaxially stretched composite composed of a soft silicone elastomer (top), a polyimide wavy network structure in a triangular lattice (middle), and another silicone elastomer (bottom) three-layer structure design. The stress-strain J-shaped curves of human skin, engineered skin composite materials, and their FEA modeling results at different locations on the human body show that their mechanical properties can accurately match the nonlinear stress-strain characteristics of human skin. Examples of applications on thin skin electrophysiological sensors that precisely match the mechanics of the human epidermis, as well as on soft hydrogel carriers that trigger drug release, suggest their broad potential use in biomedical devices.

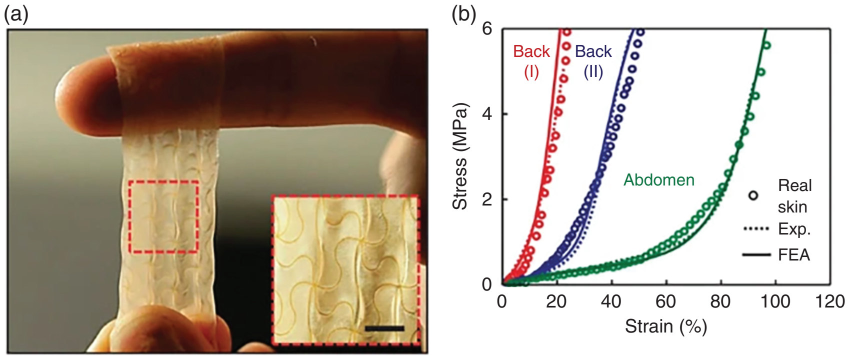

Figure 1.44 (a) A uniaxially stretched composite designed to mimic the non-linear stress-strain behavior of human skin, featuring a three-layer structure: a soft silicone elastomer (top), a polyimide wavy network (middle), and an identical silicone elastomer (bottom). (b) The stress-strain responses of human skin and the engineered composite, along with FEA modeling results, are compared across different body locations and individuals, demonstrating the material's ability to replicate skin mechanics. Source: Jang et al. [70]/Springer Nature/CC BY 4.0.

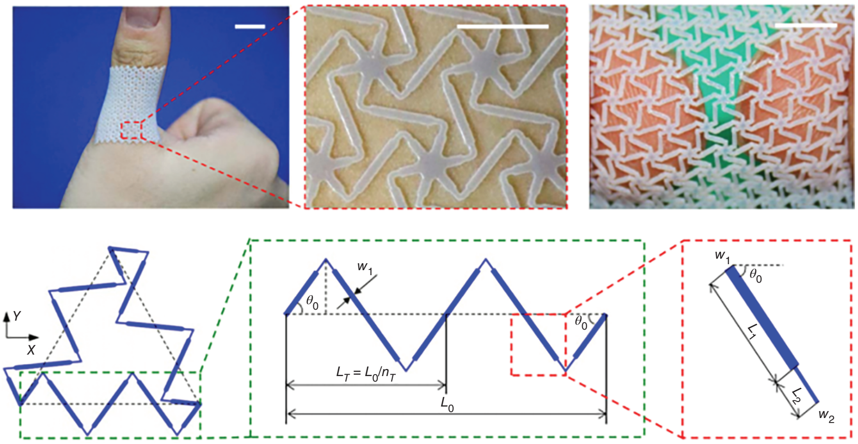

Figure 1.45 Soft network material design. Nature Publishing Group. Source: Liu and Zhang [71]/with permission of Royal Society of Chemistry.

Matching the Poisson's ratio of the network substrate to the skin can improve system comfort, which has critical applications in biomedical devices. Liu and Zhang [71] introduced soft structural materials that can be precisely tailored to produce Poisson's ratio values from −1 to 1 in an isotropic manner with tunable strains ranging from 0% to ~90%. The design relies on a network structure in a periodic lattice topology, which contains zigzag microstructures as building blocks connecting the lattice nodes, as shown in Figure 1.45.

In addition, Liu and Zhang [72] constructed a theoretical model of infinitesimal deformation of soft network materials, which is composed of an arbitrary-shaped microstructure periodic lattice. The analytical solutions of Poisson's ratio and elastic modulus of triangle, honeycomb, and square lattice topologies were obtained based on the mechanical model. These analytical solutions elucidate the different effects of lattice topology and microstructure geometry on Poisson's ratio of network materials with designed zigzag microstructures.

1.2.3 Curvilinear Substrate Designs

Curvilinear electronic systems are often integrated with curved substrates, and the ability to pattern nonplanar substrates enables the development of devices with unique or enhanced properties, such as hemispherical cameras with reduced aberrations and broader fields of view and biomimetic pressure sensors integrated into artificial skin. However, traditional micromachining techniques, such as conventional photolithography, do not work well with curved substrates. Therefore, there has been a solid effort to develop new technologies, including micromolding, self-assembly, and surfactant-induced patterning [73].

Hemispherical substrates are one of the most widely studied curved substrates because of their essential applications in imaging systems compared to the traditional flat case. Digital camera systems with bionic designs can offer certain

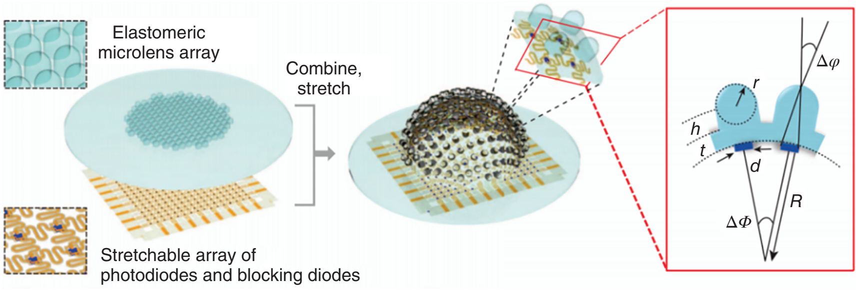

Figure 1.46 Schematic diagram of the components and integration solution of a digital camera in the form of a hemispherical, counter-positioned compound eye. Source: Song et al. [75]/with permission of Springer Nature.

advantages in imaging compared to conventional devices. Use photodetector arrays on a hemispherical surface, like the retina of the mammalian eye, rather than the standard flat layout [74]. Based on the wide-angle field of view, low aberration, high motion understanding, and infinite depth of field of arthropods, Song et al. [75] combined elastic composite optical elements with a deformable array of thin silicon photodetectors into an integrated system. The integrated piece can be transformed from the fabricated planar geometry to a hemispherical shape for integration into an opposing camera, as shown in Figure 1.46.

Another advantage of hemispherical imaging systems is their ability to match strongly nonplanar image surfaces (Petzval surfaces), thus creating new design options. Although these systems have advantages over traditional planar designs, their fixed detector curvature makes them incompatible with changes in the Petzval surface that accompany variable zoom achieved with simple lenses. Jung et al. [76] designed a class of digital imaging devices that overcome this limitation by using a photodetector array on a thin elastic membrane capable of reversibly deforming into a hemispherical shape with a radius of curvature that can be dynamically adjusted via hydraulic pressure. Combining this type of detector with a similar adjustable fluid plano-convex lens results in a hemispherical camera with variable zoom and excellent imaging properties.

Deformable curved substrates can also be adapted to complex surfaces encountered in biology to enable conformal integration with stretchable electronic systems. Stretchable electronics have been applied to balloon catheters to enable efficient ablation, surface-integrated tactile sensing, and complete conformal contact with the endocardial surface, thereby eliminating cardiac subsidence caused by blood flow around its surface [77]. A key challenge is to achieve biocompatible interfaces between semiconductor and sensor technology categories and the soft and curved surfaces of the body. Kim et al. developed a solution based on biocompatible materials and equipment that is directly integrated with the elastic membrane of a traditional balloon catheter, as shown in Figure 1.47. Connecting a variety of stretchable functional sensors and actuators in an array layout renders their operation immune to the significant strain deformations associated with repeated expansion/contraction. These concepts have the potential to find application in

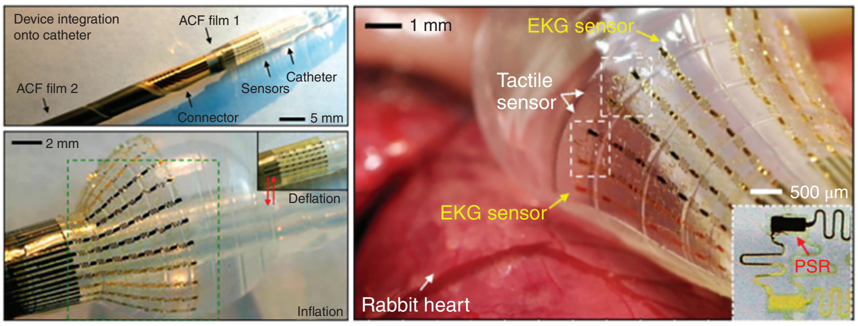

Figure 1.47 Optical image of a multifunctional inflatable balloon catheter integrating tactile and electrographic sensors. Source: Kim et al. [78]/with permission of Springer Nature.

future surgical systems, not only catheter-based ones but also on other platforms such as surgical gloves [78].

1.3 Structural Designs for Spatial Integration of Device Systems

Stretchable electronics in 3D forms have received increasing attention in recent years because of the enhanced level of integration and the new functionalities enabled by spatial layouts. Such systems have the potential to offer the performance of conventional wafer-based technologies. Still, they can be stretched like a rubber band, twisted like a rope, bent over a pencil, and folded like paper [79]. This section highlights a few representative structural designs in this context, covering the strategies of folding-based origami, buckling-guided 3D assembly, and stacked multilayer assembly [7].

1.3.1 Strategy of Folding-Based Origami

Origami and kirigami, the ancient techniques for making paperworks of art, can be a promising strategy to overcome driving 3D fabrication at the micro-/nanoscale. In this strategy, traditional planar techniques can quickly produce 2D components and 3D structures are constructed by folding each 2D part to specific orientations. In this way, not only will the advantages of existing planar techniques, such as high precision, programmable patterning, and mass production, be preserved, but the fabrication capability will also be significantly expanded without complex and expensive equipment modification/development [80] (Figure 1.48).

Recent work [81] demonstrates the utility of the methods of origami/kirigami and conceptually related schemes in cutting, folding, and buckling in the construction of devices for emerging classes of technologies, with examples in mechanical/optical metamaterials, stretchable/conformable electronics, micro-/nanoscale biosensors, and large-amplitude actuators. Specific notable progress is deploying functional materials such as single-crystal silicon, shape memory polymers, energy-storage

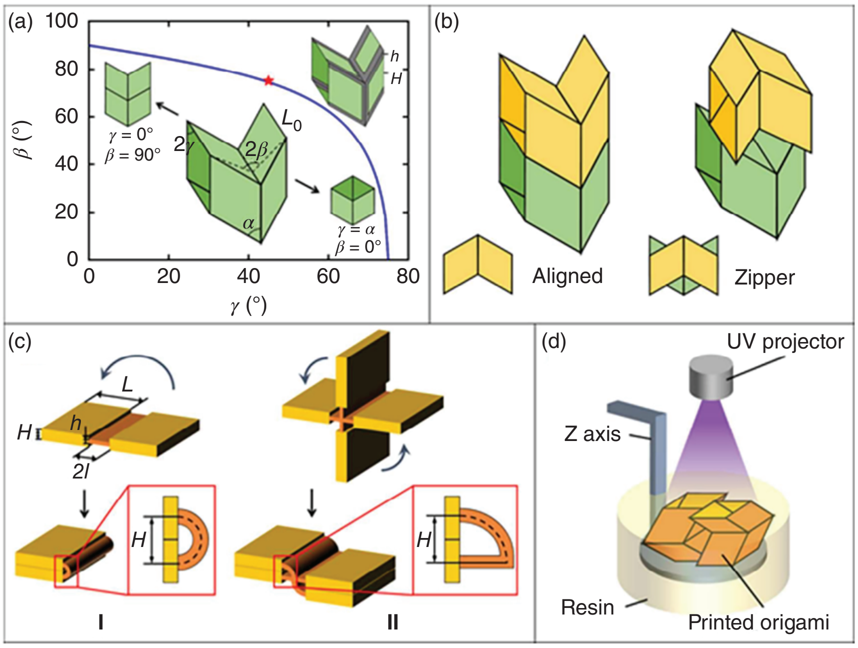

Figure 1.48 (a) Geometry of the origami tube unit (variation of the half dihedral angle β through the folding process; the red star marks the initial half dihedral angle β0 for the 3D-printed origami tubes). (b) A schematic illustration of the aligned tubes and zipper-coupled origami tubes. (c) The geometry of thick origami hinges. (d) A schematic figure for the DLP 3D printer. Source: Zhao et al. [79]/with permission of Royal Society of Chemistry.

materials, and graphene into elaborate three-dimensional micro- and nanoscale architecture.

Miskin et al. [82] from Cornell University bond graphene sheets to nanometer-thick layers of glass to make ultrathin bimorph actuators that bend to micrometer radii of curvature in response to small strain differentials. These strains are two orders of magnitude lower than the fracture threshold for the device, thus maintaining conductivity across the structure. By patterning 2-μm-thick rigid panels on top of bimorphs, we localize bending to the unpatterned regions to produce folds. Although the graphene bimorphs are only nanometers thick, they can lift these panels, the weight equivalent of a 500-nm-thick silicon chip.

By a rational configuration design with a versatile laser processing strategy, graphene-based hydroelectric generators (GHEGs) of sophisticated architectures with diversified functions such as rollable, stretchable, and even multidimensional transformation are achieved by Yang et al. [83] at Tsinghua University. More importantly, a wide range of 3D deformable generators that can automatically assemble and transform from planar geometries into spacial architectures are also successfully fabricated, including cubic boxes, pyramids, Miura-ori, and footballs. These GHEGs demonstrate excellent electricity-generation performance in curling and elongating states. The generated voltages are quickly up to 1.5 V under humidity

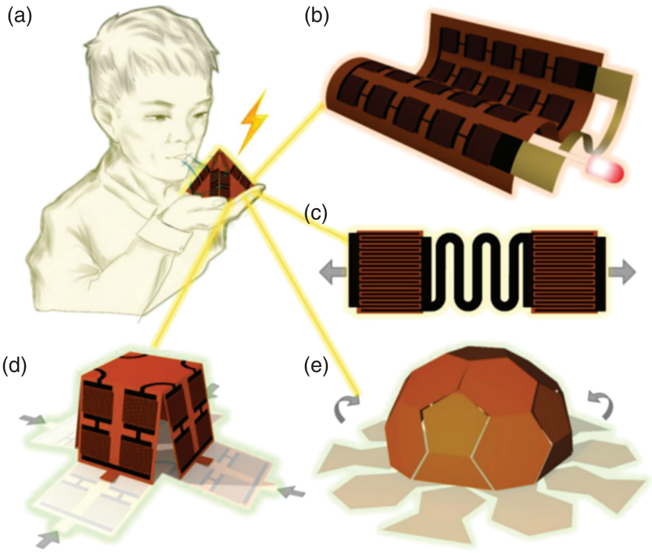

Figure 1.49 (a) Schematic diagram of GHEGs with excellent deformation ability, which can generate electricity when the relative humidity changes. (b) A large-scale, rollable GHEG integration. (c) Stretchable GHEGs with serpentine bridge–island structure. The 3D deformable configuration of (d) cube and (e) football structure. Source: Yang et al. [83]/with permission of John Wiley & Sons.

variation in the atmosphere, powering various commercial electronic components. These deformable GHEGs can be applied on complicated surfaces, human bodies, and many more beyond those demonstrated in their work (Figures 1.49 and 1.50).

Arizona State University [84] has demonstrated an example of origami-enabled silicon solar cells and showed that this solar cell can reach up to 644% areal compactness while maintaining reasonably good performance upon cyclic folding/unfolding. This approach opens an alternative direction of producing flexible, stretchable, and deformable electronics (Figure 1.51).

Rojas et al. [85] from King Abdullah University of Science and Technology described two affordable and flexible thermoelectric nanogenerators (TEGs) developed on paper substrates using simple micromachining and microfabrication techniques. Moreover, they exhibit mechanical stability and adaptability (through folding and cutting techniques) for a diverse set of scenarios where vertical or horizontal schemes can be conveniently used depending on the final application (Figure 1.52).

Kim et al. [86] demonstrates fully integrated, bezel-less transistor arrays using stretchable origami substrates and foldable conducting interconnects. Reversible folding of these arrays is enabled by origami substrates, which are composed of rigid support fixtures and foldable elastic joints. In addition, hybrid structures of thin metal films and metallic nanowires worked as foldable interconnects, which are located on the elastomeric joints.

Ji et al. [87] reports an unconventional approach to form photo-patternable, transparent cellulose nanofiber (CNF) hybrid films as flexible and stretchable

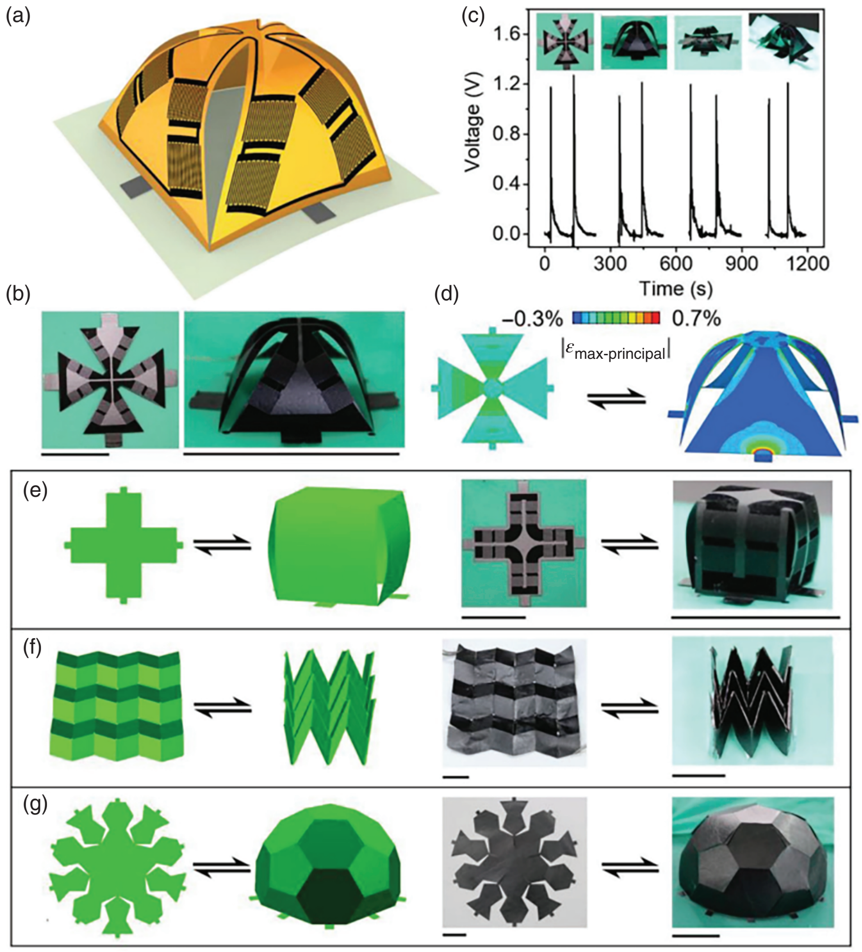

Figure 1.50 (a) Schematic diagram of 3D-GHEG assembled into a pyramid structure. (b) Optical images of pyramidal 3D-GHEG formed by planar GO film in the expansion (left) and assembly (right) states. (c) Voc of pyramidal 3D-GHEG under expanded, assembled, uniaxially stretched, and contracted states. (d) FEA results that describe the formation of pyramid 3D-GHEG in the expanded state (left) and the assembled state (right), corresponding to the optical images in (b). FEA simulation results and the corresponding experimental images of (e) cubic box, (f) Miura-ori, and (g) half-football structure in the initial state (left panel) and the assembled state (right panel). Scale bars: 20 mm. Source: Yang et al. [83]/with permission of John Wiley & Sons.

substrates to improve device reliability using simultaneous electrospinning and spraying. Furthermore, exploiting its photo-patternability, reversible foldability and stretchability, origami forms of the substrate can be produced by integrating the CNF patterns with elastomeric joints. They demonstrate flexible touchscreen panels and transparent organic light-emitting diodes (TOLEDs) using a CNF hybrid film, providing evidence for its potential and widespread application in flexible and stretchable electronics.

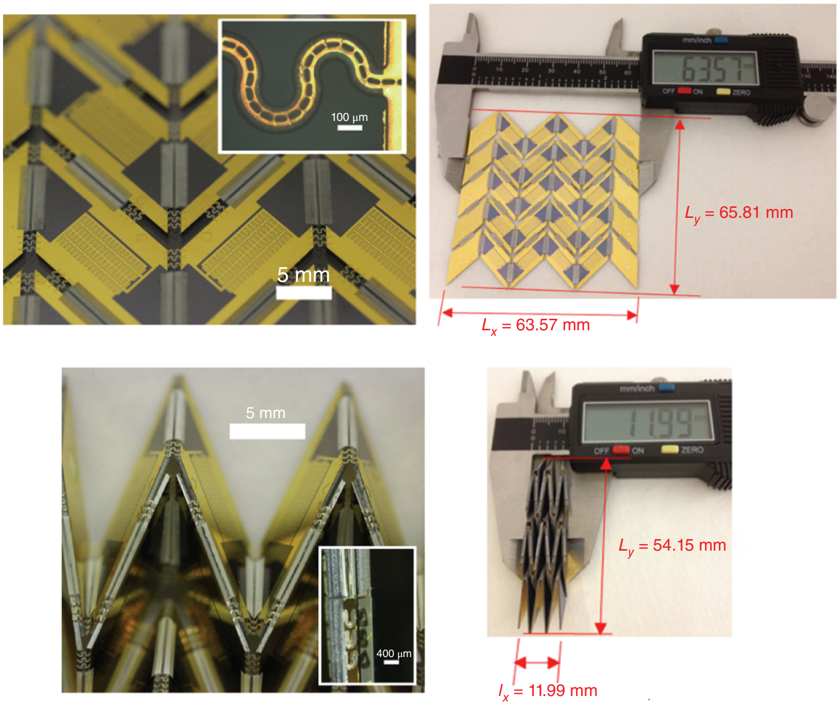

Figure 1.51 Optical pictures of the fabricated origami-enabled Si solar cells and measured dimensions of the origami-enabled Si solar cells. Source: Tang et al. [84]/with permission of AIP Publishing.

Schenk and Guest [88] from the Guest University of Pennsylvania, Philadelphia, PA, described two folded metamaterials based on the Miura-ori fold pattern. First, a folded shell structure is introduced, where the fold pattern provides a negative Poisson's ratio for in-plane deformations and a positive Poisson's ratio for out-of-plane bending. Second, a cellular metamaterial is described based on the stacking of individual folded layers, where the folding kinematics are compatible between layers. Additional freedom in the metamaterial design can be achieved by varying the fold pattern within each layer.

A Miura unit cell mentioned is shown in Figure 1.53. Its geometry can be parameterized in a few ways [89–93]. They define the unit cell by the dimensions of its most minor constituent component, a parallelogram with sides a and b and acute angle $\boldsymbol{\varphi}$, and the angles between the planes are denoted as θ_A and θ_Z. For a selected set of outer dimensions H, S, V, and L, the fold pattern parameters can then be back-calculated.

Cheng et al. [94] prepared total cells using $Li_4Ti_5O_{12}$ and $LiCoO_2$ powders deposited onto current collectors of paper coated with carbon nanotubes. Folded cells showed higher areal capacities than the planar versions, with a 5 × 5 cell folded using the Miura-ori pattern displaying a 14× increase in areal energy density, as shown in Figure 1.54.

Lin et al. [95] demonstrates a simple and low-cost paper-based photodetector array featuring superior deformability using printable ZnO nanowires, carbon

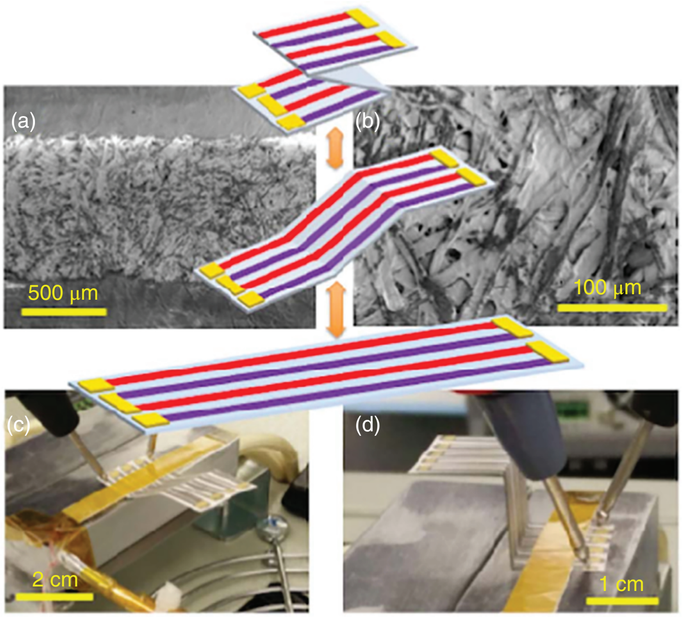

Figure 1.52 Structure and photographs of the TEGs. (a) Scanning electron microscopy (SEM) image of a strip of Bi$_2$Te$_3$-deposited on standard paper. (b) Zoom-in SEM image of (a). Standard paper-based foldable TEG with four thermoelectric pairs, (c) top view, and (d) side view. (In the middle, a schematic representation of the foldable paper-based TEG). Source: Rojas et al. [85]/with permission of Elsevier.

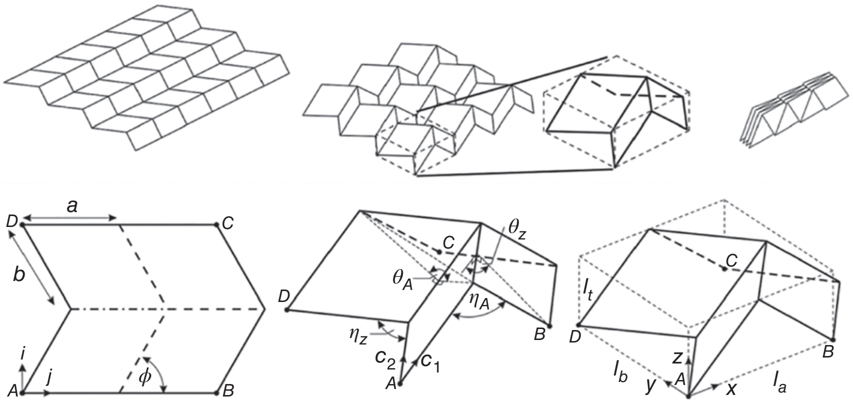

Figure 1.53 A folded Miura-ori sheet consists of tessellations of a unit cell. The unit cell geometry can be described using parameters defining a parallelogram facet, a, b, φ, and angles θ_A and θ_Z. Source: Mohammadsalehi and Mostofinejad [92]/with permission of Elsevier.

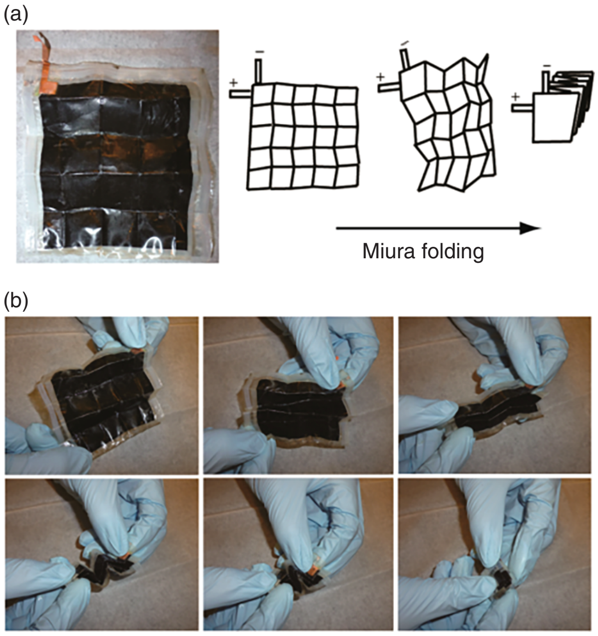

Figure 1.54 (a) Schematic of Miura folding procedures for 5 × 5 pattern and photographs of 6 cm × 7 cm battery sealed in Parylene-C (unfolded state). (b) Photos of Miura folding to compact the battery to its folded state. Source: Cheng et al. [94]/with permission of American Chemical Society.

electrodes, and origami-based techniques. With a folded Miura structure, the paper photodetector array can be oriented in four directions via tessellated parallelograms to provide excellent omnidirectional light harvesting capabilities. Additionally, they demonstrate that the device can be repeatedly stretched (up to 1000% strain), bent (bending angle ±30°), and twisted (up to 360°) without degrading performance because of the paper-folding technique, which enables the ZnO nanowire layers to remain rigid even as the device is deformed.

1.3.2 Strategy of Buckling-Guided 3D Assembly

Compared to folding-based origami strategies, recently developed assembly methods guided by controlled buckling can access more sophisticated 3D geometries, owing to the versatility of complex deformation modes, precursor designs, and loading strategies. These methods apply to a broad set of material types (e.g. metal, semiconductor, soft polymers) and feature scales (e.g. from nanometers to centimeters) because of the full compatibility with conventional microfabrication technologies [96–99] (Figure 1.55).

Guo et al. [100] establishes methods of controlled mechanical assembly as versatile routes to three-dimensional (3D) mesostructures from patterned 2D films. Previously reported schemes use pre-stretched elastomeric substrates as assembly platforms to induce compressive buckling of 2D precursor structures, thereby

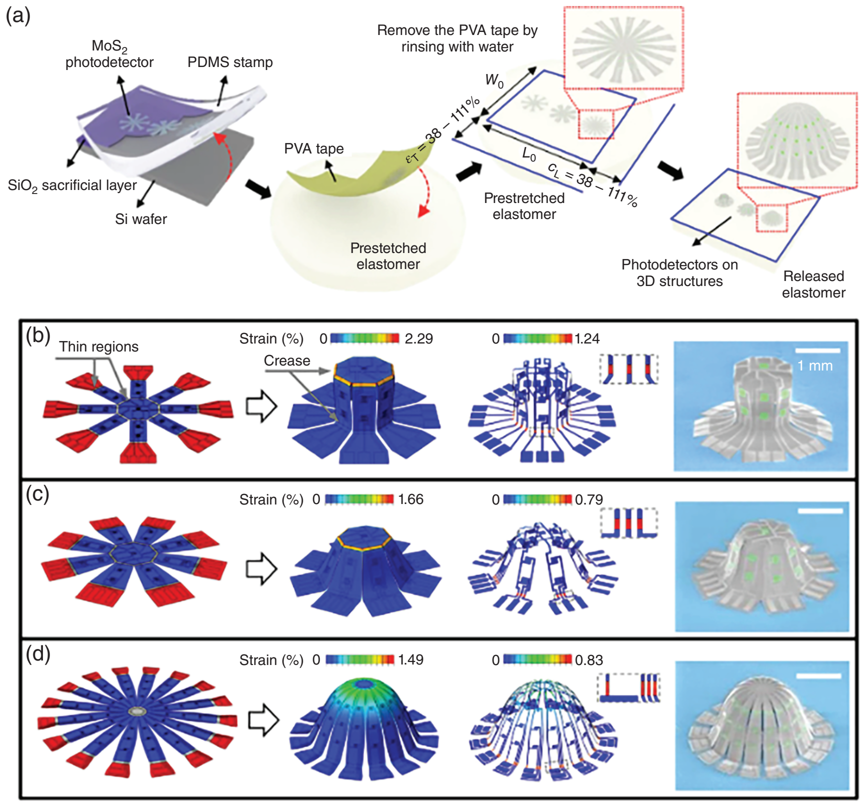

Figure 1.55 (a–d) Assembly and mechanical analysis of 3D photodetector structures from 2D materials. A schematic illustration of processes for fabricating the 3D systems. Source: Lee et al. [99]/Springer Nature/CC BY 4.0.

enabling their controlled transformation into 3D architectures. They introduce tensile buckling as a different, complementary strategy that bypasses the need for a pre-stretched platform, thereby simplifying the assembly process and opening routes to additional classes of 3D geometries unobtainable with compressive buckling.

Adams et al. [101] demonstrated conformal printing of electrically small antennas (ESAs) onto the convex and concave surfaces of hemispherical glass substrates. Their bandwidth approaches the fundamental limit for their size, offering nearly an order of magnitude improvement over rudimentary monopole designs (Figure 1.56).

Pfeiffe et al. [102] presented a direct transfer patterning process, which allows metallic patterns to be stamped onto a contoured substrate. This process made some of the most efficient ESAs while maintaining bandwidths approaching the physical limit. Liu et al. [103] introduced a mechanically guided 3D assembly approach for the design and fabrication of deformable hemispherical ESAs that can offer tunable, dynamic properties to adapt to changes in environmental conditions. The strategy exploits controlled compressive buckling of strategically patterned 2D precursor structures as a low-cost and high-yield scheme using conventional,

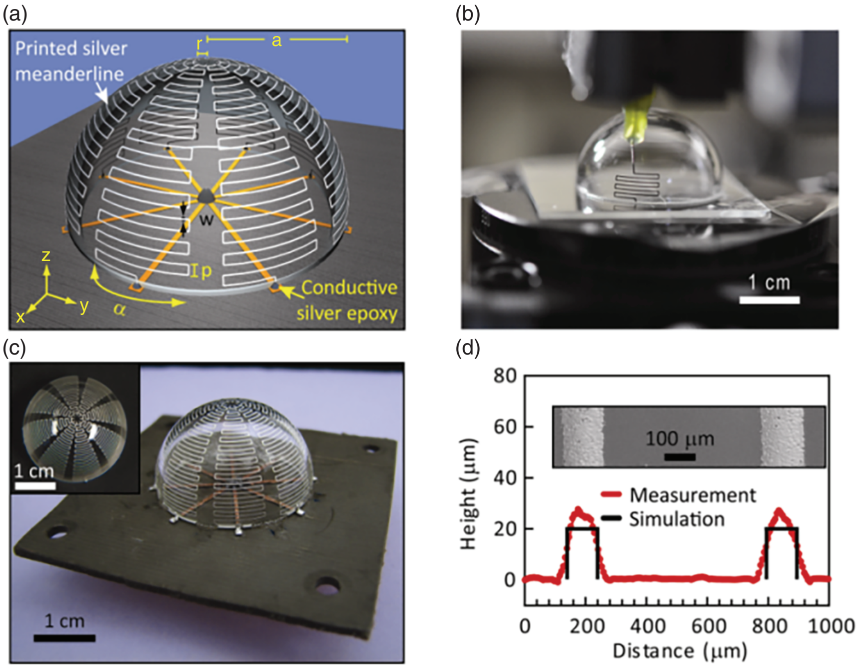

Figure 1.56 (a) Illustrates an electrically small antenna with labeled geometric parameters. (b) Optical image of an antenna during the printing process. (c) Optical images of a completed antenna (ESA1) in side and top (inset) views. (d) Optical profilometry scan of representative meanderings on ESA1 with the background surface subtracted and scanning electron micrograph of these features (inset). Source: Adams et al. [101]/with permission of John Wiley & Sons.

planar processing technologies, and commercially available platforms. Combined numerical simulations and experimental measurements show outstanding performance characteristics regarding the quality factor and radiation efficiency. Application of external tensile strains to elastomeric substrates for these systems allows them to be reshaped and reversibly tuned through a wide range of center frequencies. Mechanical testing under different loading conditions demonstrates the ability of these ESAs to accommodate large deformations. Jobs et al. [104] presents a novel microfluidic three-dimensional ESA. It is easy to construct simply by pneumatically inflating a planar stretchable liquid alloy microfluidic antenna into a spherical cap. Its center frequency is tuned when it is grown (Figure 1.57).

Fu et al. [105] introduced concepts for morphable 3D mesostructures in diverse materials and fully formed planar devices spanning length scales from micrometers to millimeters. The approaches rely on elastomer platforms deformed in different time sequences to elastically alter the 3D geometries of supported mesostructures via nonlinear mechanical buckling. Over 20 examples have been experimentally and theoretically investigated, including mesostructures that can be reshaped between different geometries as well as those that can morph into three or more distinct states (Figure 1.58).

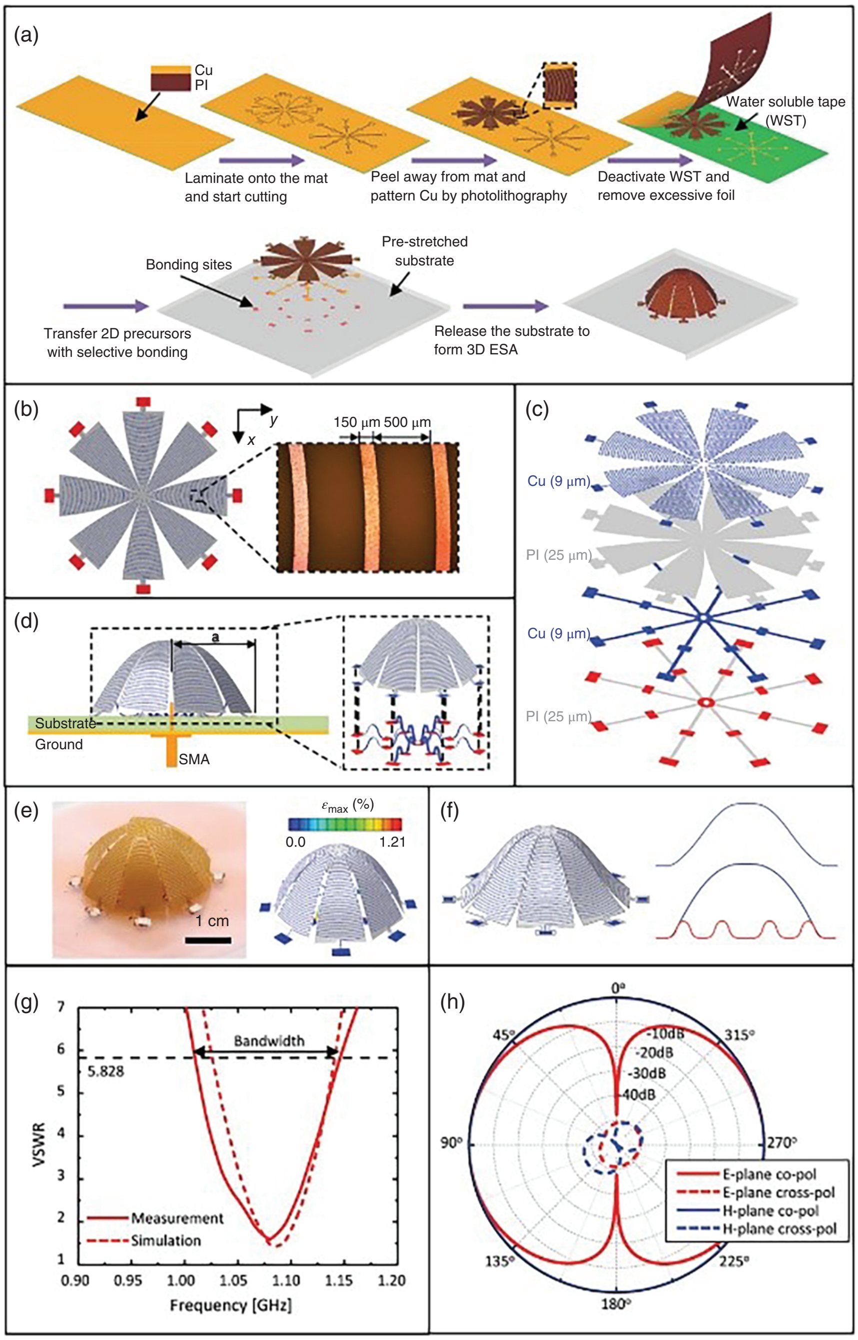

Figure 1.57 (a–h) Design, fabrication, experimental measurements, and numerical simulations of meander line-based hemispherical electrically small antennas (MHESAs). Source: Liu et al. [103]/with permission of John Wiley & Sons.

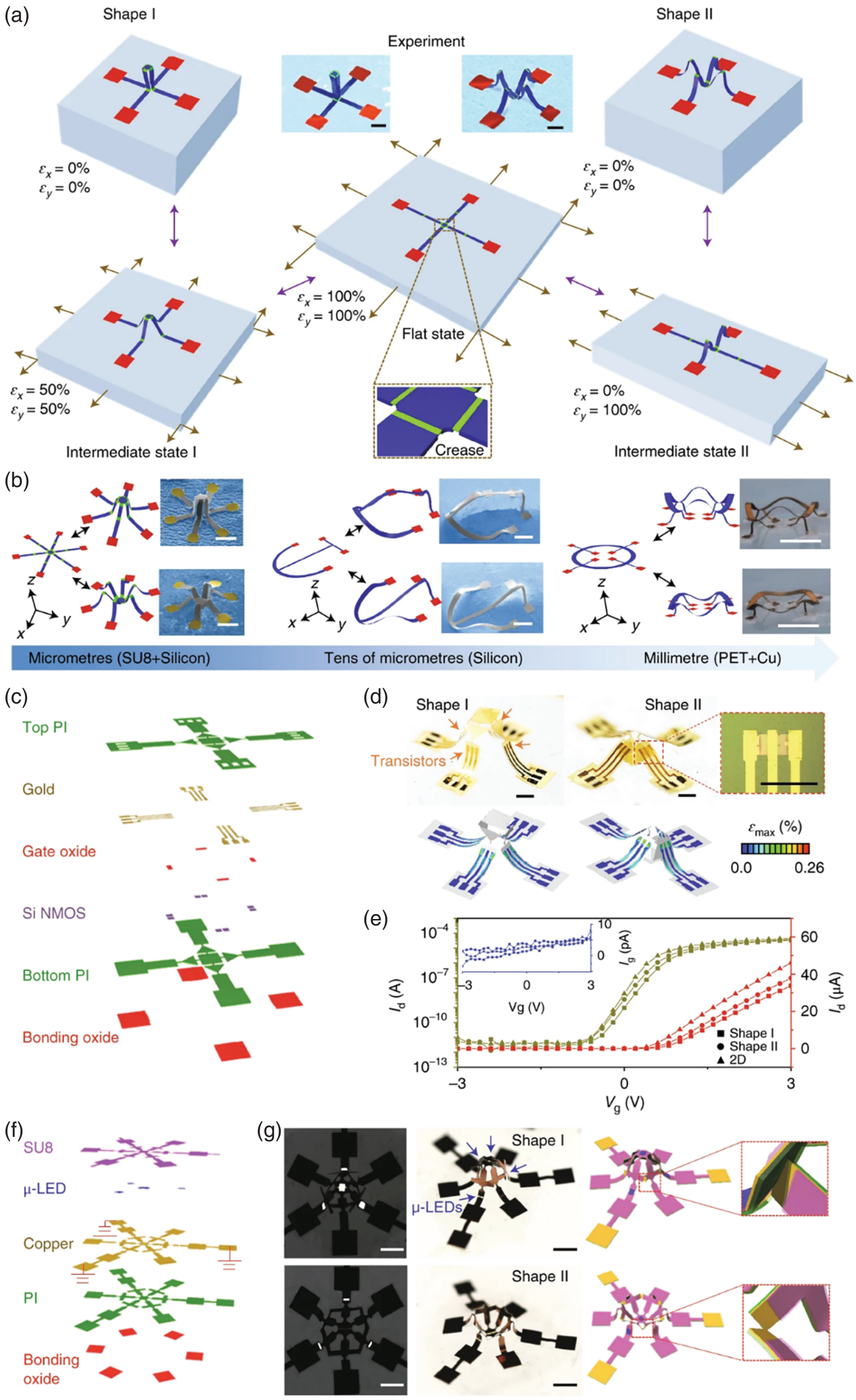

Figure 1.58 Morphable 3D mesostructures and integrated circuits by loading-path controlled mechanical assembly. Source: Fu et al. [105]/with permission of Springer Nature.

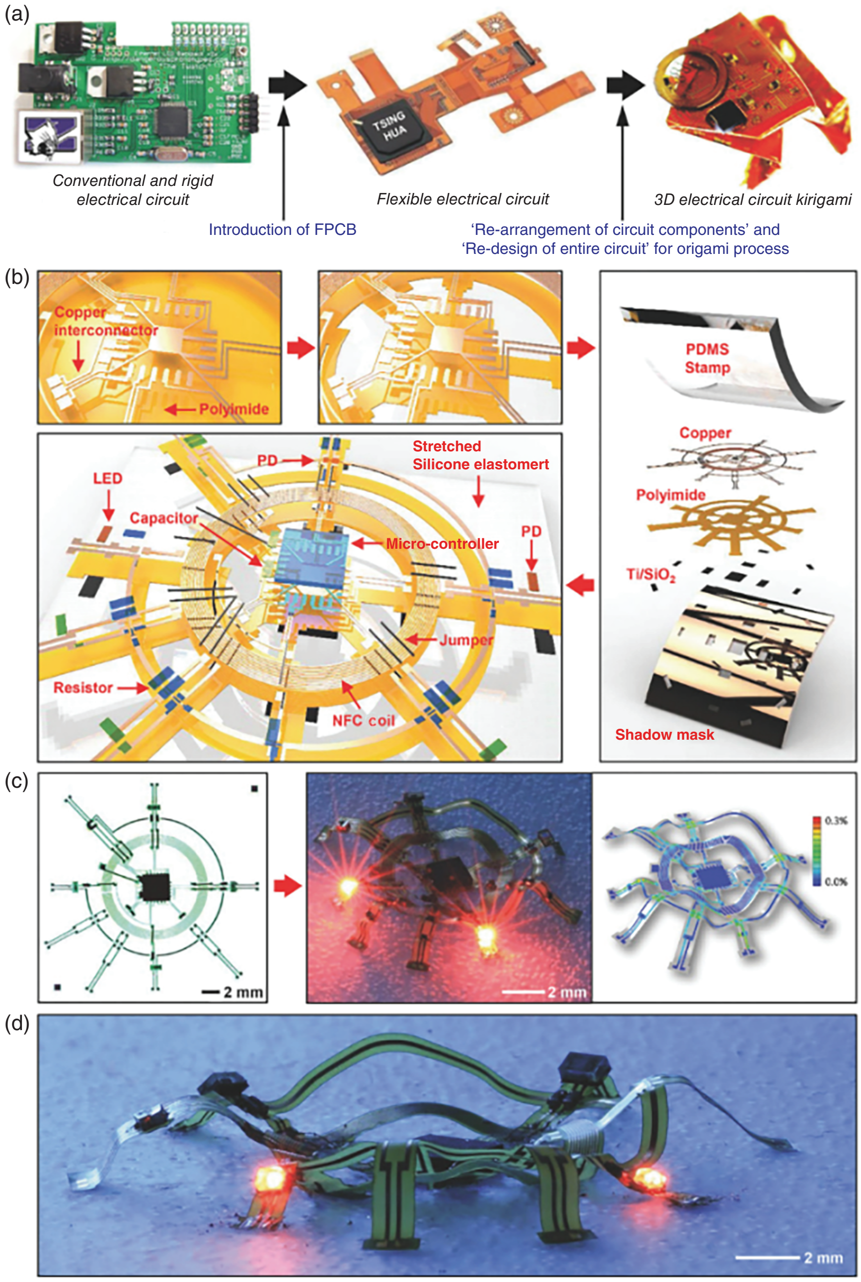

Figure 1.59 (a–d) Materials and procedures for assembly of 3D electronic/optoelectronic systems starting from conventional 2D flexible printed circuit board (FPCB) technology. Source: Kim et al. [106]/with permission of John Wiley & Sons.

Kim et al. [106] described deterministic assembly processes for transforming conventional, planar devices based on flexible printed circuit board (FPCB) platforms into those with 3D architectures in a manner that is fully compatible with off-the-shelf packaged or unpackaged parts. The strategy involves mechanically guided geometry transformation by out-of-plane buckling motions following controlled forces imposed at precise locations across the FPCB substrate by a pre-stretched elastomer platform. The geometries and positions of cuts, slits, and openings defined in the FPCB provide additional design parameters to control the final 3D layouts. The mechanical tunability of the resulting 3D FPCB platforms, afforded by elastic deformations of the substrate, allows these electronic systems to operate in an adaptable manner [106] (Figure 1.59).

Ling et al. [107] reports a simple, general, and effective route to 3D hierarchical architectures of cellular graphene with desired geometries using a mechanically guided 3D assembly approach to overcome the two challenges. Demonstrations include more than ten 3D hierarchical architectures with diverse configurations, ranging from mixed tables and tents, to double-floor helices, to kirigami-/origami-inspired structures, and to fully separated multilayer architectures. The LED arrays interconnected with 3D helical coils and 3D interdigital supercapacitors fabricated with solid-state electrolytes provide prototypic examples of wearable devices that exhibit outstanding electromechanical properties and can maintain stable performances with little change in the electrical and electrochemical responses under extreme deformations (Figure 1.60).

1.3.3 Stacked Multilayer Designs

Minimizing the size of the device system and maximizing the integration density of the circuits represents a challenge for stretchable inorganic electronics. Integration of the functional components into stacked multilayer designs could address the limitation of available density that can be reached using the conventional single-layer design [7, 108, 109]. Scholars presented some results, forming the basis of soft, skin-compatible means for efficient photovoltaic generation and high-capacity storage of electrical power using dual-junction, compound semiconductor solar cells, and chip-scale, rechargeable lithium-ion batteries, respectively. Miniaturized

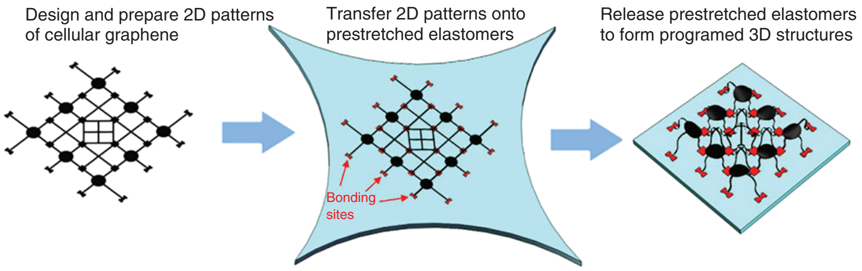

Figure 1.60 Mechanically guided, deterministic assembly of 3D hierarchical structures of cellular graphene. Source: Ling et al. [107]/with permission of American Chemical Society.

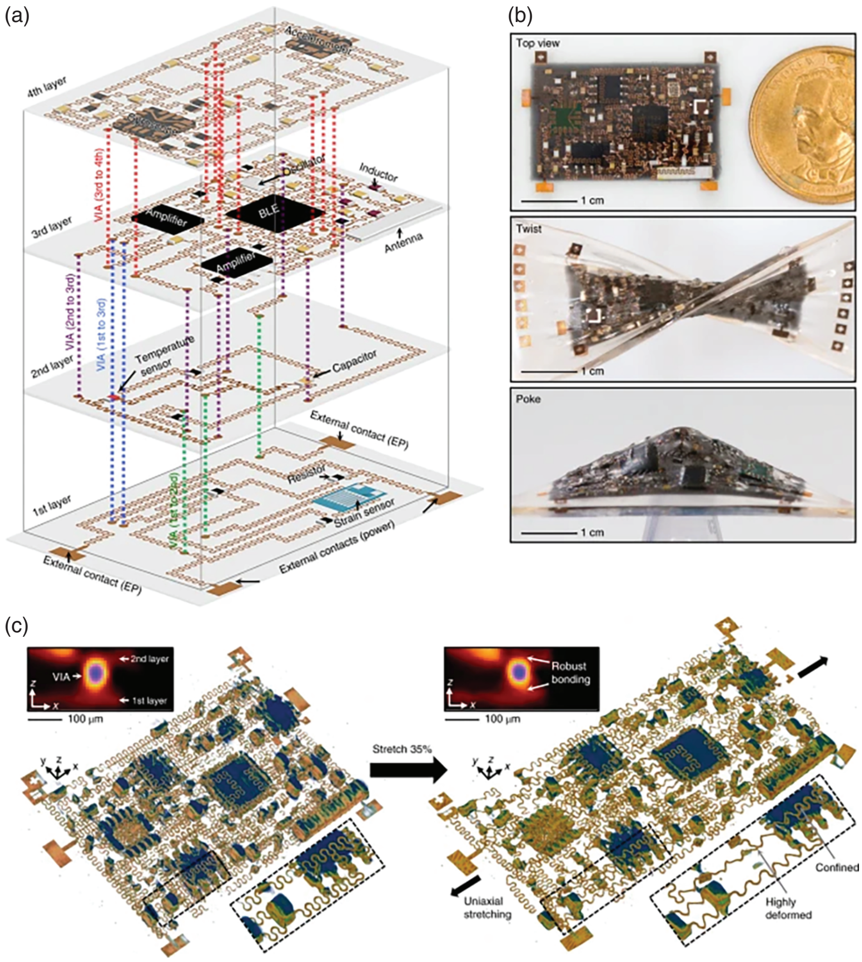

Figure 1.61 (a–c) Design and characterization of a four-layer stretchable system. Source: Huang et al. [110]/with permission of Springer Nature.

components, deformable interconnects, optimized array layouts, dual-composition elastomer substrates, superstrates, and encapsulation layers represent vital features. Systematic studies of the materials and mechanics identify optimized designs, including unusual configurations that exploit a folded, multilayer construct to improve the functional density without adversely affecting the soft, stretchable characteristics.

Huang et al. [110] reports a framework for engineering three-dimensional integrated stretchable electronics by combining strategies in material design and advanced microfabrication. Three-dimensional devices are built layer by layer by transferring pre-designed stretchable circuits on elastomers and creating vertical interconnect accesses using laser ablation and controlled soldering. Their approach enables a higher integration density on stretchable substrates than single-layer approaches and allows new functionalities that would be difficult to implement with conventional single-layer designs. Using this engineering framework, we create a stretchable human–machine interface testbed that is based on a four-layer design and offers eight-channel sensing and Bluetooth data communication capabilities (Figure 1.61).

References

1 Yoder, M.A., Yan, Z., Han, M. et al. (2018). Semiconductor nanomembrane materials for high-performance soft electronic devices. *Journal of the American Chemical Society* 140 (29): 9001–9019. https://doi.org/10.1021/jacs.8b04225.

2 Song, J., Jiang, H., Choi, W.M. et al. (2008). An analytical study of two-dimensional buckling of thin films on compliant substrates. *Journal of Applied Physics* 103 (1): 2548. https://doi.org/10.1063/1.2828050.

3 Rogers, J.A., Lagally, M.G., and Nuzzo, R.G. (2011). Synthesis, assembly and applications of semiconductor nanomembranes. *Nature* 477 (7362): 45–53. https://doi.org/10.1038/nature10381.

4 Sun, Y. and Rogers, J.A. (2007). Inorganic semiconductors for flexible electronics. *Advanced Materials* 19 (15): 1897–1916. https://doi.org/10.1002/adma.200602223.

5 Kim, D.-H., Ahn, J.-H., Choi, W.M. et al. (2008). Stretchable and foldable silicon integrated circuits. *Science* 320 (5875): 507–511. https://doi.org/10.1126/science.1154367.

6 Baca, A.J., Ahn, J.-H., Sun, Y. et al. (2008). Semiconductor wires and ribbons for high- performance flexible electronics. *Angewandte Chemie International Edition* 47 (30): 5524–5542. https://doi.org/10.1002/anie.200703238.

7 Xue, Z., Song, H., Rogers, J.A. et al. (2020). Mechanically-guided structural designs in stretchable inorganic electronics. *Advanced Materials* 32 (15): 1902254. https://doi.org/10.1002/adma.201902254.

8 Khang, D.-Y., Rogers, J.A., and Lee, H.H. (2009). Mechanical buckling: mechanics, metrology, and stretchable electronics. *Advanced Functional Materials* 19 (10): 1526–1536. https://doi.org/10.1002/adfm.200801065.

9 Yang, S., Khare, K., and Lin, P.-C. (2010). Harnessing surface wrinkle patterns in soft matter. *Advanced Functional Materials* 20 (16): 2550–2564. https://doi.org/10.1002/adfm.201000034.

10 Yu, C., Wang, Z., Yu, H. et al. (2009). A stretchable temperature sensor based on elastically buckled thin film devices on elastomeric substrates. *Applied Physics Letters* 95 (14): 141912. https://doi.org/10.1063/1.3243692.

11 Yu, C. and Jiang, H. (2010). Forming wrinkled stiff films on polymeric substrates at room temperature for stretchable interconnects applications. *Thin Solid Films* 519 (2): 818–822. https://doi.org/10.1016/j.tsf.2010.08.106.

12 Zhang, Q. and Yin, J. (2018). Spontaneous buckling-driven periodic delamination of thin films on soft substrates under large compression. *Journal of the*

Mechanics and Physics of Solids 118: 40–57. https://doi.org/10.1016/j.jmps.2018.05.009.

13 Ma, Y., Xue, Y., Jang, K.-I. et al. (2016). Wrinkling of a stiff thin film bonded to a pre-strained, compliant substrate with finite thickness. *Proceedings of the Royal Society A: Mathematical, Physical and Engineering Sciences* 472 (2192): 20160339. https://doi.org/10.1098/rspa.2016.0339.

14 Yan, Z.G., Wang, B.L., and Wang, K.F. (2019). Stretchability and compressibility of a novel layout design for flexible electronics based on bended wrinkle geometries. *Composites Part B: Engineering* 166: 65–73. https://doi.org/10.1016/j.compositesb.2018.11.123.

15 Jiang, H., Khang, D.-Y., Song, J. et al. (2007). Finite deformation mechanics in buckled thin films on compliant supports. *Proceedings of the National Academy of Sciences* 104 (40): 15607–15612. https://doi.org/10.1073/pnas.0702927104.

16 Cheng, H., Zhang, Y., Hwang, K.-C. et al. (2014). Buckling of a stiff thin film on a pre-strained bi-layer substrate. *International Journal of Solids and Structures* 51 (18): 3113–3118. https://doi.org/10.1016/j.ijsolstr.2014.05.012.

17 Cheng, H. and Song, J. (2014). A simply analytic study of buckled thin films on compliant substrates. *Journal of Applied Mechanics* 81 (2): 024501. https://doi.org/10.1115/1.4025306.

18 Song, J., Jiang, H., Liu, Z.J. et al. (2008). Buckling of a stiff thin film on a compliant substrate in large deformation. *International Journal of Solids and Structures* 45 (10): 3107–3121. https://doi.org/10.1016/j.ijsolstr.2008.01.023.

19 Jiang, H., Sun, Y., Rogers, J.A. et al. (2007). Mechanics of precisely controlled thin film buckling on elastomeric substrate. *Applied Physics Letters* 90 (13): 133119. https://doi.org/10.1063/1.2719027.

20 Jiang, H., Khang, D.-Y., Fei, H. et al. (2008). Finite width effect of thin-films buckling on compliant substrate: experimental and theoretical studies. *Journal of the Mechanics and Physics of Solids* 56 (8): 2585–2598. https://doi.org/10.1016/j.jmps.2008.03.005.

21 Chen, C., Tao, W., Liu, Z.J. et al. (2011). Controlled buckling of thin film on elastomeric substrate in large deformation. *Theoretical and Applied Mechanics Letters* 1 (2): 021001. https://doi.org/10.1063/2.1102101.

22 Song, J., Huang, Y., Xiao, J. et al. (2009). Mechanics of noncoplanar mesh design for stretchable electronic circuits. *Journal of Applied Physics* 105 (12): 123516. https://doi.org/10.1063/1.3148245.

23 Li, R., Li, M., Su, Y. et al. (2013). An analytical mechanics model for the island-bridge structure of stretchable electronics. *Soft Matter* 9 (35): 8476. https://doi.org/10.1039/c3sm51476e.

24 Ko, H.C., Shin, G., Wang, S. et al. (2009). Curvilinear electronics formed using silicon membrane circuits and elastomeric transfer element. *Small* 5 (23): 2703–2709. https://doi.org/10.1002/smll.200900934.

25 Wang, A., Avila, R., and Ma, Y. (2017). Mechanics design for buckling of thin ribbons on an elastomeric substrate without material failure. *Journal of Applied Mechanics* 84 (9): 094501. https://doi.org/10.1115/1.4037149.

26 Wang, B. and Wang, S. (2016). Adhesion-governed buckling of thin-film electronics on soft tissues. *Theoretical and Applied Mechanics Letters* 6 (1): 6–10. https://doi.org/10.1016/j.taml.2015.11.010.

27 Wang, S., Xiao, J., Song, J. et al. (2010). Mechanics of curvilinear electronics. *Soft Matter* 6 (22): 5757. https://doi.org/10.1039/c0sm00579g.

28 Yang, X.-D., Yang, S., Qian, Y.-J. et al. (2016). Modal analysis of the gyroscopic continua: comparison of continuous and discretized models. *Journal of Applied Mechanics* 83 (8): 084502. https://doi.org/10.1115/1.4033752.

29 Widlund, T., Yang, S., Hsu, Y.-Y. et al. (2014). Stretchability and compliance of freestanding serpentine-shaped ribbons. *International Journal of Solids and Structures* 51 (23–24): 4026–4037. https://doi.org/10.1016/j.ijsolstr.2014.07.025.

30 Son, D., Koo, J.H., Song, J.-K. et al. (2015). Stretchable carbon nanotube charge-trap floating-gate memory and logic devices for wearable electronics. *ACS Nano* 9 (5): 5585–5593. https://doi.org/10.1021/acsnano.5b01848.

31 Yang, S., Ng, E., and Lu, N. (2015). Indium Tin Oxide (ITO) serpentine ribbons on soft substrates stretched beyond 100%. *Extreme Mechanics Letters* 2: 37–45. https://doi.org/10.1016/j.eml.2015.01.010.

32 Fan, Z., Zhang, Y., Ma, Q. et al. (2016). A finite deformation model of planar serpentine interconnects for stretchable electronics. *International Journal of Solids and Structures* 91: 46–54. https://doi.org/10.1016/j.ijsolstr.2016.04.030.

33 Xiao, L., Zhu, C., Xiong, W. et al. (2018). The conformal design of an island-bridge structure on a nondevelopable surface for stretchable electronics. *Micromachines* 9 (8): 392. https://doi.org/10.3390/mi9080392.

34 Xu, L., Gutbrod, S.R., Bonifas, A.P. et al. (2014). 3D multifunctional integumentary membranes for spatiotemporal cardiac measurements and stimulation across the entire epicardium. *Nature Communications* 5 (1): 3329. https://doi.org/10.1038/ncomms4329.

35 Zhang, Y., Xu, S., Fu, H. et al. (2013). Buckling in serpentine microstructures and applications in elastomer-supported ultra-stretchable electronics with high areal coverage. *Soft Matter* 9 (33): 8062. https://doi.org/10.1039/c3sm51360b.

36 Zhang, Y., Wang, S., Li, X. et al. (2014). Experimental and theoretical studies of serpentine microstructures bonded to prestrained elastomers for stretchable electronics. *Advanced Functional Materials* 24 (14): 2028–2037. https://doi.org/10.1002/adfm.201302957.

37 Su, Y., Ping, X., Yu, K.J. et al. (2017). In-Plane deformation mechanics for highly stretchable electronics. *Advanced Materials* 29 (8): 1604989. https://doi.org/10.1002/adma.201604989.

38 Pan, T., Pharr, M., Ma, Y. et al. (2017). Experimental and theoretical studies of serpentine interconnects on ultrathin elastomers for stretchable electronics. *Advanced Functional Materials* 27 (37): 1702589. https://doi.org/10.1002/adfm.201702589.

39 Lv, C., Yu, H., and Jiang, H. (2014). Archimedean spiral design for extremely stretchable interconnects. *Extreme Mechanics Letters* 1: 29–34.

40 Yuan, X. and Wang, Y. (2023). Nonlinear stretching mechanics of planar Archimedean-spiral interconnects for flexible electronics. *Thin-Walled Structures* 185: 110568.

41 Huang, K., Dinyari, R., Lanzara, G. et al. (2007). An approach to cost-effective, robust, large-area electronics using monolithic silicon. 2007 IEEE International Electron Devices Meeting. IEEE, 2007, pp. 217-220.

42 Sung, W.L., Chen, C., Huang, K. et al. (2015). Development of a large-area chip network with multidevice integration using a stretchable electroplated copper spring. *Journal of Micromechanics and Microengineering* 26 (2): 025003.

43 Alcheikh, N., Shaikh, S.F., and Hussain, M. (2018). Ultra-stretchable Archimedean interconnects for stretchable electronics. *Extreme Mechanics Letters* 24: 6–13.

44 Rojas, J.P., Arevalo, A., Foulds, I.G. et al. (2014). Design and characterization of ultra-stretchable monolithic silicon fabric. *Applied Physics Letters* 105 (15).

45 Rehman, M.U. and Rojas, J.P. (2017). Optimization of compound serpentine–spiral structure for ultra-stretchable electronics. *Extreme Mechanics Letters* 15: 44–50.

46 Xu, S., Yan, Z., Jang, K.I. et al. (2015). Assembly of micro/nanomaterials into complex, three-dimensional architectures by compressive buckling. *Science* 347 (6218): 154–159.

47 Yan, Z., Han, M., Yang, Y. et al. (2017). Deterministic assembly of 3D mesostructures in advanced materials via compressive buckling: a short review of recent progress. *Extreme Mechanics Letters* 11: 96–104.

48 Liu, Y., Yan, Z., Lin, Q. et al. (2016). Guided formation of 3D helical mesostructures by mechanical buckling: analytical modeling and experimental validation. *Advanced Functional Materials* 26 (17): 2909–2918.

49 Li, K., Cheng, X., Zhu, F. et al. (2019). A generic soft encapsulation strategy for stretchable electronics. *Advanced Functional Materials*.

50 Viventi, J., Kim, D.H., Vigeland, L. et al. (2011). Flexible, foldable, actively multiplexed, high-density electrode array for mapping brain activity in vivo. *Nature Neuroscience* 14 (12): 1599–1605.

51 Jang, K., Li, K., Chung, H. et al. (2017). Self-assembled three dimensional network designs for soft electronics. *Nature Communications* 8: 15849.

52 Fan, J.A., Yeo, W.H., Su, Y. et al. (2014). Fractal design concepts for stretchable electronics. *Nature Communications* 5 (1): 3266.

53 Xu, S., Zhang, Y., Cho, J. et al. (2013). Stretchable batteries with self-similar serpentine interconnects and integrated wireless recharging systems. *Nature Communications* 4 (1): 1543.

54 Zhang, Y., Fu, H., Xu, S. et al. (2014). A hierarchical computational model for stretchable interconnects with fractal-inspired designs. *Journal of the Mechanics and Physics of Solids* 72: 115–130.

55 Zhang, Y., Fu, H., Su, Y. et al. (2013). Mechanics of ultra-stretchable self-similar serpentine interconnects. *Acta Materialia* 61 (20): 7816–7827.

56 Ma, Q. and Zhang, Y. (2016). Mechanics of fractal-inspired horseshoe microstructures for applications in stretchable electronics. *Journal of Applied Mechanics* 83 (11): 111008.

57 Xu, L., Gutbrod, S.R., Ma, Y. et al. (2015). Materials and fractal designs for 3D multifunctional integumentary membranes with capabilities in cardiac electrotherapy. *Advanced Materials* 27 (10): 1731–1737.

58 Norton, J.J.S., Lee, D.S., Lee, J.W. et al. (2015). Soft, curved electrode systems capable of integration on the auricle as a persistent brain–computer interface. *Proceedings of the National Academy of Sciences* 112 (13): 3920–3925.

59 Kim, J., Lee, M., Shim, H.J. et al. (2014). Stretchable silicon nanoribbon electronics for skin prosthesis. *Nature Communications* 5 (1): 5747.

60 Hattori, Y., Falgout, L., Lee, W. et al. (2014). Multifunctional skin-like electronics for quantitative, clinical monitoring of cutaneous wound healing. *Advanced Healthcare Materials* 3 (10): 1597–1607.

61 Liu, Z., Cheng, H., and Wu, J. (2014). Mechanics of solar module on structured substrates. *Journal of Applied Mechanics* 10 (1115/1): 4026472.

62 Lee, J., Wu, J., Ryu, J.H. et al. (2012). Stretchable semiconductor technologies with high areal coverages and strain-limiting behavior: demonstration in high-efficiency dual-junction GaInP/GaAs photovoltaics. *Small* 8: 1851–1856. https://doi.org/10.1002/smll.201102437.

63 Cantarella, G., Costanza, V., Ferrero, A. et al. (2018). Design of engineered elastomeric substrate for stretchable active devices and sensors. *Advanced Functional Materials* https://doi.org/10.1002/adfm.201705132.

64 Zhao, Q., Liang, Z., Lu, B. et al. (2018). Toothed Substrate Design to Improve Stretchability of Serpentine Interconnect for Stretchable Electronics. *Advanced Materials Technologies* 3: https://doi.org/10.1002/admt.201800169.

65 Yu, Q., Chen, F., Li, M., and Cheng, H. (2017). Buckling analysis of stiff thin films suspended on a substrate with tripod surface relief structure. *Applied Physics Letters* 111: https://doi.org/10.1063/1.5003792.

66 Qi, D., Liu, Z., Yu, M. et al. (2015). Highly stretchable gold nanobelts with sinusoidal structures for recording electrocorticograms. *Advanced Materials* 27: 3145–3151. https://doi.org/10.1002/adma.201405807.

67 Lee, Y.K., Jang, K., Ma, Y. et al. (2017). Chemical sensing systems that utilize soft electronics on thin elastomeric substrates with open cellular designs. *Advanced Functional Materials* 27: https://doi.org/10.1002/adfm.201605476.

68 Chen, H., Zhu, F., Jang, K.-I. et al. (2018). The equivalent medium of cellular substrate under large stretching, with applications to stretchable electronics. *Journal of the Mechanics and Physics of Solids* 120: 199–207. https://doi.org/10.1016/j.jmps.2017.11.002.

69 Zhu, F., Xiao, H., Xue, Y. et al. (2018). Anisotropic mechanics of cellular substrate under finite deformation. *Journal of Applied Mechanics* 85: https://doi.org/10.1115/1.4039964.

70 Jang, K.-I., Chung, H.U., Xu, S. et al. (2015). Soft network composite materials with deterministic and bio-inspired designs. *Nature Communications* https://doi.org/10.1038/ncomms7566.

71 Liu, J. and Zhang, Y. (2017). Soft network materials with isotropic negative Poisson's ratios over large strains. *Soft Matter* 14: 693–703. https://doi.org/10.1039/c7sm02052j.

72 Liu, J. and Zhang, Y. (2018). A mechanics model of soft network materials with periodic lattices of arbitrarily shaped filamentary microstructures for tunable Poisson's ratios. *Journal of Applied Mechanics* 85: https://doi.org/10.1115/1.4039374.

73 Petruczok, C.D. and Gleason, K.K. (2012). Initiated chemical vapor deposition-based method for patterning polymer and metal microstructures on curved substrates. *Advanced Materials* 24: 6445–6450. https://doi.org/10.1002/adma.201201975.

74 Shin, G., Jung, I., Malyarchuk, V. et al. (2010). Micromechanics and advanced designs for curved photodetector arrays in hemispherical electronic-eye cameras. *Small* 6: 851–856. https://doi.org/10.1002/smll.200901350.

75 Song, Y.M., Xie, Y., Malyarchuk, V. et al. (2013). Digital cameras with designs inspired by the arthropod eye. *Nature* 497: 95–99. https://doi.org/10.1038/nature12083.

76 Jung, I., Xiao, J., Malyarchuk, V. et al. (2011). Dynamically tunable hemispherical electronic eye camera system with adjustable zoom capability. *Proceedings of the National Academy of Sciences* 108: 1788–1793. https://doi.org/10.1073/pnas.1015440108.

77 Su, Y., Liu, Z., Wang, S. et al. (2014). Mechanics of stretchable electronics on balloon catheter under extreme deformation. *International Journal of Solids and Structures* 51: 1555–1561. https://doi.org/10.1016/j.ijsolstr.2014.01.008.

78 Kim, D.-H., Lu, N., Ghaffari, R. et al. (2011). Materials for multifunctional balloon catheters with capabilities in cardiac electrophysiological mapping and ablation therapy. *Nature Materials* 10: 316–323. https://doi.org/10.1038/nmat2971.

79 Zhao, Z., Kuang, X., Wu, J. et al. (2018). 3D printing of complex origami assemblages for reconfigurable structures. *Soft Matter* 14 (39): 8051–8059.

80 Ning, X., Wang, X., Zhang, Y. et al. (2018). Assembly of advanced materials into 3D functional structures by methods inspired by origami and kirigami: a review. *Advanced Materials Interfaces* 5 (13): 1800284.

81 Liu, Z., Cui, A., Li, J. et al. (2019). Folding 2D structures into 3D configurations at the micro/nanoscale: principles, techniques, and applications. *Advanced Materials* 31 (4): 1802211.

82 Miskin, M.Z., Dorsey, K.J., Bircan, B. et al. (2018). Graphene-based bimorphs for micron-sized, autonomous origami machines. *Proceedings of the National Academy of Sciences* 115 (3): 466–470.

83 Yang, C., Huang, Y., Cheng, H. et al. (2019). Rollable, stretchable, and reconfigurable graphene hygroelectric generators. *Advanced Materials* 31 (2): 1805705.

84 Tang, R., Huang, H., Tu, H. et al. (2014). Origami-enabled deformable silicon solar cells. *Applied Physics Letters* 104 (8): 083501.

85 Rojas, J.P., Conchouso, D., Arevalo, A. et al. (2017). Paper-based origami flexible and foldable thermoelectric nanogenerator. *Nano Energy* 31: 296–301.

86 Kim, M., Park, J., Ji, S. et al. (2016). Fully-integrated, bezel-less transistor arrays using reversibly foldable interconnects and stretchable origami substrates. *Nanoscale* 8 (18): 9504–9510.

87 Ji, S., Hyun, B.G., Kim, K. et al. (2016). Photo-patternable and transparent films using cellulose nanofibers for stretchable origami electronics. *NPG Asia Materials* 8 (8): e299–e299.

88 Schenk, M. and Guest, S.D. (2013). Geometry of Miura-folded metamaterials. *Proceedings of the National Academy of Sciences* 110 (9): 3276–3281.

89 Wu, W. and You, Z. (2010). Modelling rigid origami with quaternions and dual quaternions. *Proceedings of the Royal Society of London. Series A: Mathematical and Physical Sciences* 466: 2155–2174.

90 Stachel, H. (2010). A kinematic approach to Kokotsakis meshes. *Computer Aided Geometric Design* 27: 428–437.

91 Schenk, M., Allwood, J.M., and Guest, S.D. (2011). Cold gas-pressure folding of Miura-ori sheets. Steel Research International, Special Issue Proceedings of the International Conference on Technology of Plasticity (ICTP) 2011, pp 459–464.

92 Mohammadsalehi, A. and Mostofinejad, D. (2023). Behavior of high-performance concrete canvas Miura-origami structures under flexural loading. *Structures* 54: 928–945.

93 Korte, A.P., Starostin, E.L., and van der Heijden, G.H.M. (2011). Triangular buckling patterns of twisted inextensible strips. *Proceedings of the Royal Society of London. Series A: Mathematical and Physical Sciences* 467: 285–303.

94 Cheng, Q., Song, Z., Ma, T. et al. (2013). Folding paper-based lithium-ion batteries for higher areal energy densities. *Nano Letters* 13 (10): 4969–4974.

95 Lin, C.H., Tsai, D.S., Wei, T.C. et al. (2017). Highly deformable origami paper photodetector arrays. *ACS Nano* 11 (10): 10230–10235.

96 Zhang, K., Jung, Y.H., Mikael, S. et al. (2017). Origami silicon optoelectronics for hemispherical electronic eye systems. *Nature Communications* 8 (1): 1782.

97 Shi, Y., Zhang, F., Nan, K. et al. (2017). Plasticity-induced origami for assembly of three dimensional metallic structures guided by compressive buckling. *Extreme Mechanics Letters* 11: 105–110.

98 Zhang, Y., Zhang, F., Yan, Z. et al. (2017). Printing, folding and assembly methods for forming 3D mesostructures in advanced materials. *Nature Reviews Materials* 2: 17019.

99 Lee, W., Liu, Y., Lee, Y. et al. (2018). Two-dimensional materials in functional three-dimensional architectures with applications in photodetection and imaging. *Nature Communications* 9 (1): 1417.

100 Guo, X., Wang, X., Ou, D. et al. (2018). Controlled mechanical assembly of complex 3D mesostructures and strain sensors by tensile buckling. *npj Flexible Electronics* 2 (1): 14.

101 Adams, J., Duoss, E.B., Malkowski, T.F. et al. (2011). Conformal printing of electrically small antennas on three-dimensional surfaces. *Advanced Materials* 23 (11): 1335–1340.

102 Pfeiffe, C., Xu, X., Forrest, S. et al. (2012). Direct transfer patterning of electrically small antennas onto three-dimensionally contoured substrates. *Advanced Materials* 24 (9): 1166–1170.

103 Liu, F., Chen Y, Song H et al. (2019). High performance, tunable electrically small antennas through mechanically guided 3D assembly. *Small* 15 (1): 1804055.

104 Jobs, M., Hjort, K., Rydberg, A. et al. (2013). A tunable spherical cap microfluidic electrically small antenna. *Small* 9 (19): 3230–3234.

105 Fu, H., Nan, K., Bai, W. et al. (2018). Morphable 3D mesostructures and microelectronic devices by multistable buckling mechanics. *Nature Materials* 17 (3): 268–276.

106 Kim, B.H., Liu, F., Yu, Y. et al. (2018). Electronic structures: mechanically guided post-assembly of 3D electronic systems (Adv. Funct. Mater. 48/2018). *Advanced Functional Materials* 28 (48): https://doi.org/10.1002/adfm.201870344.

107 Ling, Y., Zhuang, X., Xu, Z. et al. (2018). Mechanically assembled, three-dimensional hierarchical structures of cellular graphene with programmed geometries and outstanding electromechanical properties. *ACS Nano* 12 (12): 12456–12463.

108 Kim, B.H., Lee, J., Won, S.M. et al. (2018). Three-dimensional silicon electronic systems fabricated by compressive buckling process. *ACS Nano* 12 (5): 4164–4171.

109 Xu, R., Lee, J.W., Pan, T. et al. (2017). Designing thin, ultrastretchable electronics with stacked circuits and elastomeric encapsulation materials. *Advanced Functional Materials* 27 (4): 1604545.

110 Huang, Z., Hao, Y., Li, Y. et al. (2018). Three-dimensional integrated stretchable electronics. *Nature Electronics* 1 (8): 473–480.